17th International Symposium on Ice
Saint Petersburg, Russia, 21-25 June 2004
International Association of Hydraulic Engineering and Research

SIDE-VIEWING HIGH-SPEED VIDEO OBSERVATIONS OF ICE CRUSHING

Robert Gagnon[1]

ABSTRACT

Rectangular thick sections (1 cm thickness) of lab-grown mono-crystalline ice have been confined between two thick Lexan plates and crushed at -10^{o}C from one edge face at a rate of 1 cm/s using a stainless steel platen (1 cm thickness) inserted between the plates. The transparent Lexan plates permitted side viewing of the ice behavior during crushing and the visual data were recorded using high-speed video. An in-plane fracture occurs in the ice sample early in the tests and expands from the platen/ice contact area as load increases. Ice on one side of the in-plane fracture experiences shattering and pulverization while the ice on the other side remains intact but melts at the platen/ice contact where the pressure is high (~ 40 MPa). The continuous production and flow of liquid at high pressure in a thin layer at the intact ice / platen interface was strikingly evident and most of the load was supported in this zone. While some spalls did occur at the intact ice contact zone, cyclic spalling that normally occurs in ice crushing experiments was suppressed due to the unusual confinement arrangement. The crushing on one side of the in-plane fracture and melting on the other side occurred continuously at the nominal platen penetration rate for most of a test, however, when spalls did occur the relative platen/ice penetration rate was momentarily much higher due to the release of elastic energy in the system.

INTRODUCTION

Several studies of ice crushing behavior have been conducted over of the past few decades, driven by the need for understanding and mitigating ice hazards associated with offshore oil and gas development and transportation, and shipping in general. Some of the more recent investigations included in situ visual observations. At high strain rates visual data have been acquired from indentors (Gagnon, 1998; Fransson et al., 1991) and a ship hull (Riska et al., 1990) that incorporated windows for viewing the indented ice surface, and there have also been test apparatus that allowed viewing of the ice/indentor interface through the ice samples (Gagnon, 1994a; Gagnon and Mølgaard, 1991). The visual data, combined with displacement, load and pressure records, and

[1] Institute for Ocean Technology, National Research Council of Canada, St. John's, NF, A1B 3T5

temperature data in a few instances, have lead to significant new insights into the ice crushing process.

At low strain rates visually dramatic experiments have been performed by edge-loading confined thin sections of polycrystalline ice to demonstrate plastic deformation and recrystallization (Wilson, 1999). The present study incorporates a similar concept except that the strain rate is much higher, and is in the range associated with ice crushing rather than plastic deformation. The loads are much higher and the apparatus is correspondingly stronger. This is the first time that such a technique has been used for ice crushing. The visual data from the present side-viewing perspective corroborate with visual results from other previous experiments and help clarify any ambiguities arising from the earlier viewing perspectives.

METHOD AND APPARATUS

Figure 1a shows a conceptual schematic of the test method. The ice specimen is a 1 cm thick section. The sample is confined between two thick plates (12 cm x 13 cm 3.8 cm) of transparent acrylic (Lexan). The Lexan plates are mounted in a holder (Figure 1b), made from 19 mm thick Aluminum plate, that keeps the Lexan and ice specimen in place. The Lexan plates are separated by small plastic spacers (1 cm thick) between the plates at the sides. The holder provided confinement to the ice sample at the bottom and at the side edges to a height of 6 cm from the bottom. Notches are cut in the upper portion of the side confining plates (above 6 cm) to allow for lateral escape of crushed ice during the tests. Aluminum braces, with adjustment bolts, hold the plates together. The crushing platen was made of stainless steel and had dimensions 10 cm x 6 cm x 1 cm. When the ice holder was mounted and carefully aligned in the MTS test frame, the crushing platen could snuggly slide between the Lexan plates to make contact with the exposed edge of the ice sample. For the actual test

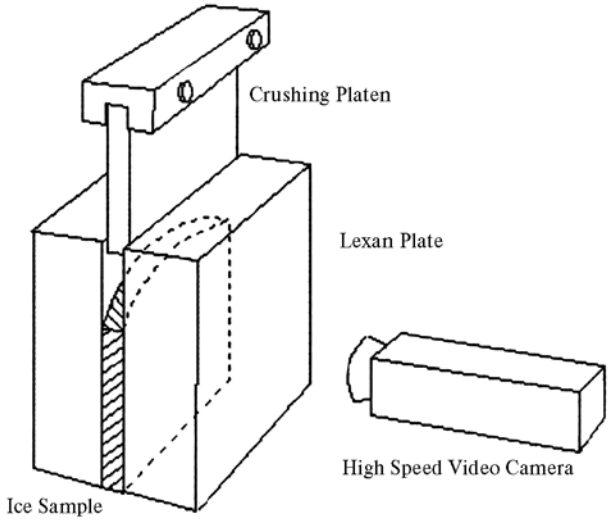

Fig. 1a.

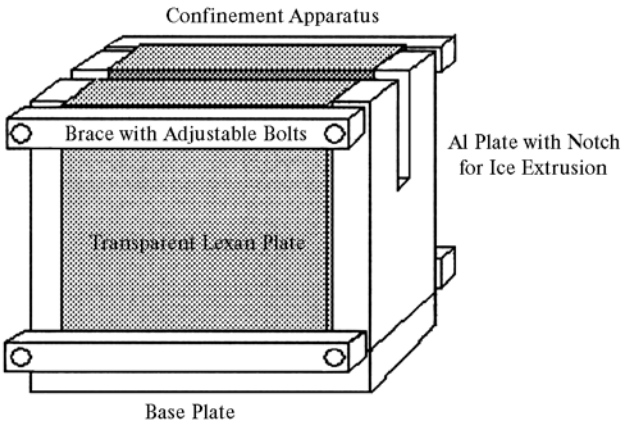

Fig. 1b.

Fig. 1. (a) Conceptual schematic of the ice crushing test method. (b) Details of the ice holder

configuration the ice holder was mounted under the test frame crosshead, and the crushing platen was mounted on the test frame actuator piston so that it slid into the ice holder from below. Hence for the test images presented below the orientation is inverted from that shown in Figure 1.

Preparation of the sample was critical to insure uniform confinement. This was achieved by first machining the ice so it could closely fit into the space between the Lexan plates. The space between the plates was filled with degassed deionzed water at 0^{o}C. The ice sample was then carefully inserted into the space, displacing water in so doing until fully inserted. Hence all the space was filled with ice primarily and a small amount of water in any gaps around the edges not filled by the ice. The ice holder, with ice sample and water, was wrapped in an insulating material exposing only the bottom plate and was then laid on a cold metal surface in the cold room at -10^{o}C. This caused the small amount of water in the holder to freeze from the bottom up enabling a perfect fit of the ice and avoiding stress associated with trapped freezing water. Once the sample was fully frozen in, its exposed top edge was rounded, by melting with a piece of warm metal, to insure that initial contact with the crushing platen occurred at the center. The ice holder and sample were then left to thermalize to -10^{o}C prior to testing.

Single crystal ice samples and iceberg ice samples were used during the test program. This paper describes the results from the tests using the single-crystal samples. The caxis for the single crystal samples is vertical and in the plane of the ice slab shown in Figure 1. The crushing platen movement rate was the same for all tests, 10 mm/s. The method of growing the large single crystals has been described by Gagnon (1994a).

A digital high-speed video camera (Photron FASTCAM) was used to record the ice behavior during the tests. The image capture rate was 500 frames /s and the resolution of the black and white images was 1280 x 1024 pixels.

ANALYSIS OF A TEST ON A SINGLE CRYSTAL SAMPLE

A series of images, with time stamps, from the video record (Figure 2) show various aspects of the test. Figure 3 is a reference figure where features of the apparatus and ice behavior discussed below are indicated for the reader's convenience. The image in Figure 3 is the same image in Figure 2 at t=0.702 s. The load record for the test is shown in Figure 4 with markers (open circles) corresponding to the 8 video images in Figure 2. Time zero corresponds to the time first contact occurs between the platen and the ice. Note that we show the record for the time up to just beyond the large spall event in Figure 2, t=1.058 s. Beyond this time the platen begins to penetrate so far into the ice holder as to start restricting the escape of pulverized ice through the egress slots cut in the side plates.

In the following description when a feature of the ice behavior is referred to in an image the feature will have occurred exactly at the time stamp on the image or some time before. This is done for presentation purposes because sometimes the feature in question is more clearly visible in a later image than when it first appears.

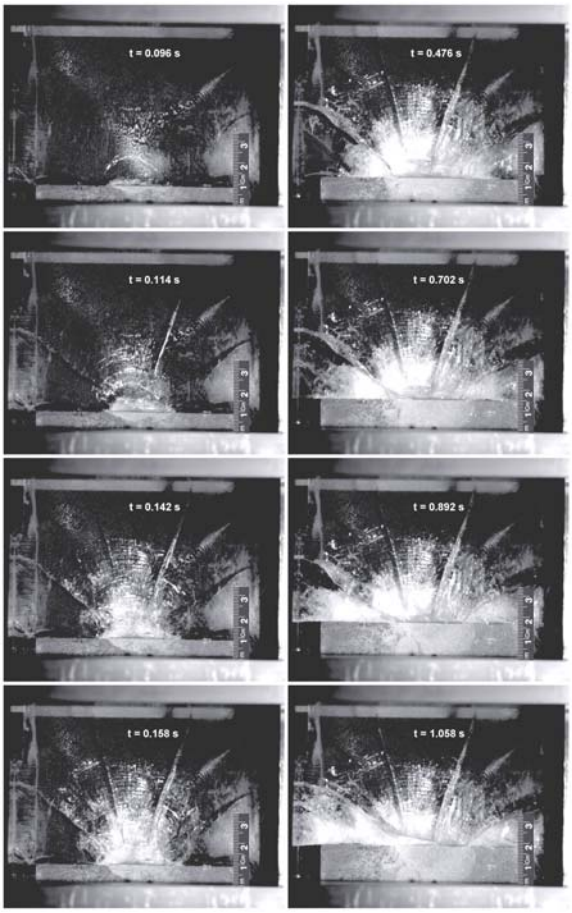

Fig. 2. High-speed video images (with time stamps) from a test using a single crystal ice specimen. The ice slab is in the plane of the image and the view is through a Lexan plate as shown in Figure 1. The rule at the lower right indicates the scale of the test and the progress of the crushing platen as it inserts between the Lexan plates from below at a nominal rate of 1 cm/s. Note that the view is inverted from the schematics shown in Figure 1. The images run downwards from the top left to the bottom right. The test was conducted at -10^{o}C

When the platen makes contact with the ice load begins to accumulate (Figure 4). The high-speed video record shows that one of the ice faces usually looses its adherence to the Lexan early in the test. As the loss of adherence progresses a fan-shaped fracture surface appears in the plane of the ice specimen (Figure 2, t=0.096 s) separating the ice that has adhered to the Lexan from the ice that has let go of the Lexan. This in-plane fracture continues to extend as the platen moves forward and is about halfway through the thickness of the ice slab. Linear out-of-plane cracks also begin to appear in a radial pattern centered at the platen/ice contact zone. The first two of these appear at the sides of the ice sample within one video frame interval, just as the ice face finishes separating from the Lexan at t=0.098 s (Figure 2, t=0.114 s). These are followed by two other out-of-plane cracks that appear one after another, 8 and 21 frames later, in the more central view area with initial lengths of about 3 cm (Figure 2, t=0.158 s). The latter extend from both ends to lengthen by 2 or 3 more centimeters over the span of a few images immediately following their appearance. Eventually the in-plane fractures at the sides of the image lead to complete separation of pieces from the ice specimen at the peak in load at around t=0.242 s in the test (Figure 2, t=0.476 s).

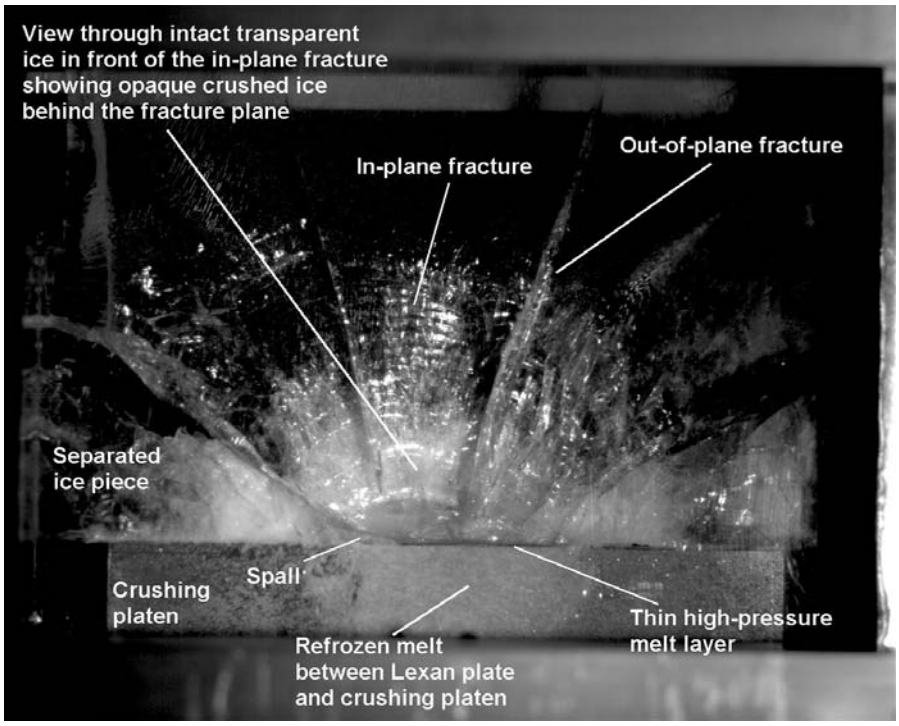

Fig. 3. Image from the high-speed video record indicating various aspects of the apparatus and ice behavior. The image is the same as that shown in Figure 2 at t=0.702 s

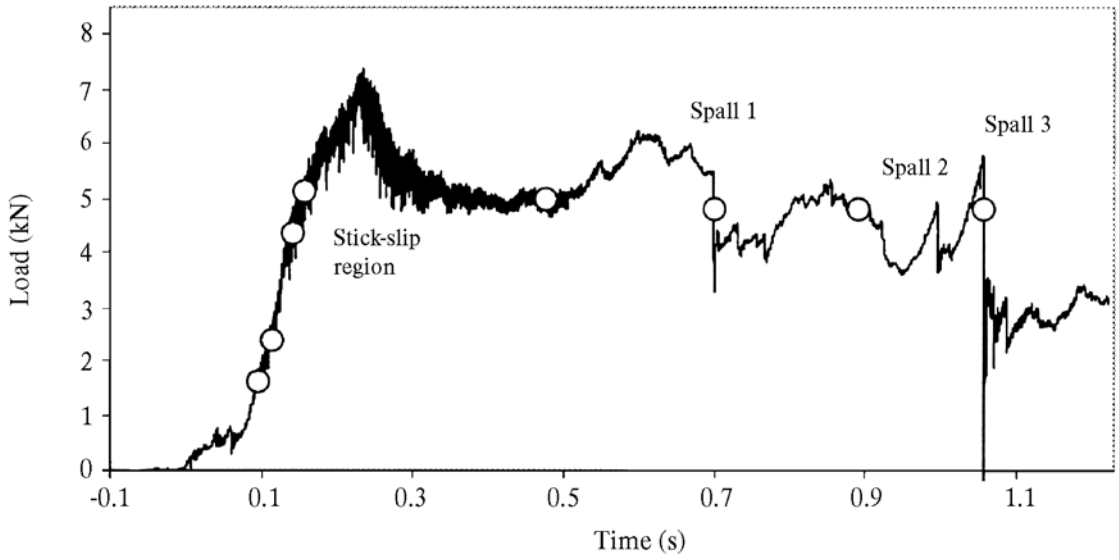

Fig. 4. Load record for the test shown in Figures 2 and 3 with markers (open circles) corresponding to the 8 video images in Figure 2. Time zero corresponds to the time first contact occurs between the crushing platen and the ice. Three spall events and a region of the record exhibiting stick-slip are also indicated on the chart. Spalls 1 and 3 correspond to the images in Figure 2 with time stamps t=0.702 s and t=1.058 s respectively

Apparently the portion of the ice sample on the backside of the large in-plane fracture (relative to the camera), with the face that has lost adherence to the Lexan, is more susceptible to fracture-generating stresses. This arises because in-plane lateral confinement is no longer provided by adherence to the Lexan or by attachment to the

rest of the ice, due to the in-plane fracture. Consequently this ice portion shatters and is pulverized as the platen moves ahead. In tests where the intact ice that remains adhered to the Lexan plate faces the camera, the movement of pulverized ice can be seen behind it, such as the test shown in Figures 2 and 3. Alternately, in some tests the pulverized ice is on the side facing the camera, and consequently it blocks the view of the behavior of the intact ice since it is opaque. Some tests were recorded for both scenarios thereby revealing the behavior of the pulverized and intact ice in detail. In the video record for the test under consideration the pulverized ice can be seen flowing away to the left and right from the central region of the ice specimen, where the pressure is higher. The remaining ice on the front side of the in-plane fracture stays relatively intact however. It is likely that the pulverized ice provides some degree of confinement that helps the intact ice remain in its undamaged state.

While the shattered and pulverized ice is removed from the contact zone by simply flowing away, a dramatically different mechanism accounts for the removal of intact ice at the ice/platen contact, namely melting. This is evident in the video record that shows a thin layer of liquid extruding from between the platen and ice interface (Figures 2 and 3). The liquid aspect of the layer is evident in that it can be seen wetting the pulverized material adjacent to the sides and behind the intact ice. The liquid can also be seen flowing from between the ice and the platen into the narrow gap between the platen and the Lexan plate in the plane of the image (Figures 2 and 3), where it then refreezes. Note that during the test setup when the platen is partially inserted between the Lexan plates, that the fit is so snug that there is a little friction between the Lexan and metal. Consequently at the end of a test a roughly semi-circular patch of extremely thin ice, transparent in its upper central area, is visible on the side of the platen where the liquid froze (Figure 5). The estimated thickness of the thin ice layer is ~ 0.3 mm. This refrozen ice causes a portion of the load record to exhibit a regular small-amplitude pattern of stick-slip (Figures 4 and 6), probably due to the repeated freezing of liquid to the platen and Lexan in the small gap and breakage of the bond as the platen moves.

Fig. 5. Crushing platen with a roughly semi-circular patch of extremely thin ice frozen to its side at the leading end following the test shown in Figure 2. The ice layer is transparent in its upper central area and is ~ 0.3 mm thick

The relative movement of the platen against the ice is continuous for most of the record shown (i.e. at the nominal test rate of 0.010 m/s) except for the instances where spalls

break away from the ice/platen contact area that cause abrupt substantial load drops to occur where the penetration rate is momentarily much higher due to the release of elastic stress in the system. Three such events are evident in the load record (Figure 4) and are shown in an expanded section in Figure 7. The images corresponding to two of the spall events are shown in Figure 2 at t=0.702 s (i.e. same as Figure 3) and at t=1.058 s, and occur at the left of the ice/platen contact zone. Spall 2 occurred on the back side of the contact zone, rather than at the left side as in the case of Spalls 1 and 3, and was therefore not as visible. We can estimate the rate of penetration during the load drops induced by the spall events from the load record and the compliance of the ice/apparatus system. The compliance of the system was estimated to be around 2×10^{-8} m/N, from the load and displacement data acquired at the end of a test when the platen was withdrawn. If we consider the load drop at Spall 3, for example, the load changed from 5700 N to 2000 N in 0.2 ms. Hence, using the compliance, we see that the platen moved against the ice 7.4×10^{-5} m in 0.2 ms, that is, at a rate at ~ 0.37 m/s during the load drop (Figure 8).

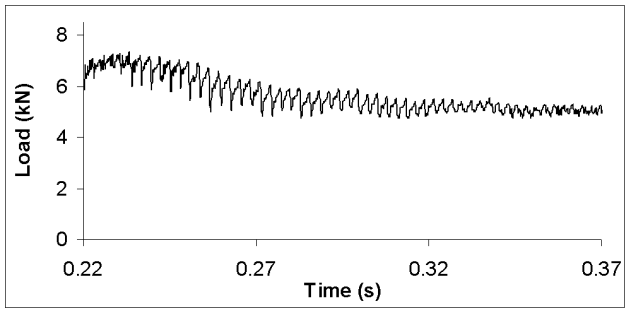

Fig. 6. Expanded view of the segment of the load record shown in Figure 4 exhibiting small-amplitude stick-slip

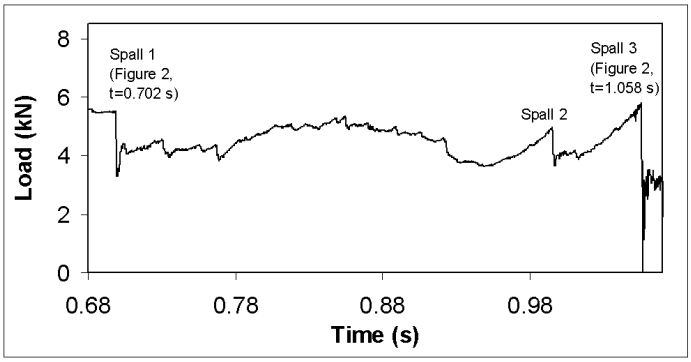

Fig. 7. Expanded view of the segment of the load record shown in Figure 4 showing three spall events. The high-speed video images in Figure 2 associated with two of the spall events are also indicated

We attach significance to spalling because it is known to be a major factor in the behavior of ice impact and indentation. The characteristic sawtooth pattern in load records from ice indentation tests (Michel and Blanchet, 1983; Evans et al., 1984; Määttänen, 1983; Timco and Jordaan, 1988; Sohdi and Morris, 1984; Frederking et al., 1990), and shape evolution of the ice contact, stems from spalling at the high pressure ice/indentor contact region (Gagnon, 1999). The distinctly different nature of the confinement in the present test configuration is probably the reason why cyclic spalling, so characteristic in previous investigations, did not occur.

The melting process has been observed before and explained in detail (Gagnon and Mølgaard, 1991; Gagnon 1994a, 1994b; Gagnon and Sinha, 1991). In the region of high pressure contact between the platen and the intact ice a pre-existing thin layer of liquid on the ice surface (Faraday, 1859), or one that is produced by pressure melting, starts to flow because of the extreme pressure. The viscous flow of the liquid generates heat and additional melting occurs immediately since the liquid layer is in direct contact with ice.

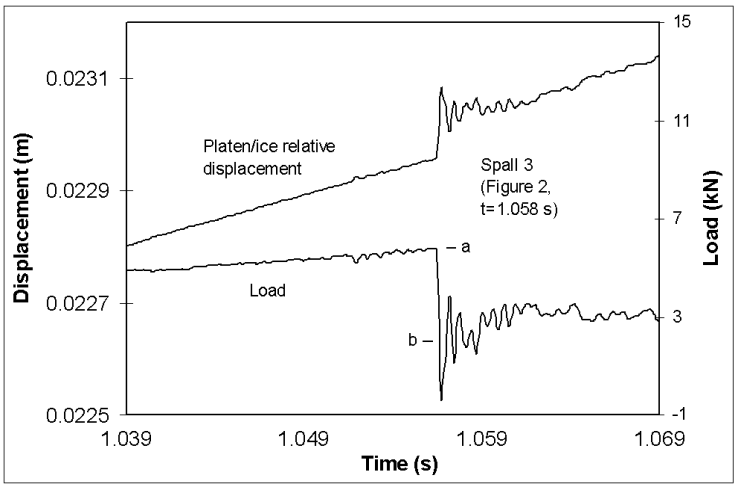

Fig. 8. Highly expanded view of the segment of the platen/ice relative displacement record (left axis) and corresponding segment of the load record (right axis) showing Spall 3. The platen/ice relative displacement was determined from the nominal platen displacement minus the load times the compliance of the system

The process can happen at relatively slow rates, such as the continuous crushing rate seen in the present load record and also at much faster rates, such as occurs during a load drop where the pressure is momentarily higher. For a given contact area the liquid layer is thicker at the higher penetration rate (Gagnon, 1994b and 1994b). In either case the integrity of the ice in the hard spot is preserved. In situ liquid layer thickness measurements have been made in crushing tests on truncated pyramids of ice at a similar scale to the present tests at a crushing platen displacement rate of 0.5 cm/s, both at load drops and during the slower rate of penetration on the ascending side of sawteeth in the load records. The layer thickness was found to be 2.8 microns for a relative penetration rate of 0.0014 m/s on the ascending side of sawteeth in the load record, and 20.8 microns for the relative penetration rate of 0.26 m/s at load drops (Gagnon, 1994b). In the present tests the relative penetration rate for the continuous crushing portion of the test is 0.010 m/s (i.e. the nominal penetration rate) and 0.37 m/s at the load drops. Hence, the high-pressure liquid layer thickness is probably similar in both sets of experiments, at least for the load drops.

We note that at larger scales, such as the previous Hobson's Choice Ice Island indentation tests (Masterson et al., 1993), the relative ice/indentor displacement during the ascending portion of the sawteeth in load was very small or none at all, that is, the actuator displacement was mostly taken up elastically in the ice/apparatus system (Gagnon, 1998). The majority of the actual ice/indentor relative displacement occurred at the load drops, caused by spall events, at a high displacement rate. These, and other characteristics, have been discussed in detail (Gagnon, 1998).

We can get a rough estimate of the pressure existing at the ice/platen interface on the intact ice from the measured load and by estimating the area of contact, assuming the pulverized ice that flows away to the sides will be supporting much less pressure. The length of the intact ice contact is clearly evident from the video record. Its thickness is estimated to be half the thickness of the ice slab (5 mm). Assuming the load is applied to this estimated contact area we obtain a pressure of about 40 MPa. This is quite consistent with in situ pressure measurements obtained from the earlier experiments

(Gagnon, 1999). To further support the assumption that the intact ice supports the majority of the load we can compare the actual measured extent of the load drops, on the charts (Figures 7 and points a and b in Figure 8), with the change in contact area of intact ice due to the spalls from the video record. We see that the load drop for Spall 1 amounts to a reduction of contact area of about 25% (Figure 2, t=0.702 s and Figure 3) that matches well with the drop in actual load, about 25%. Similarly for Spall 3 in Figure 2 at t=1.058 s, the change in area is about 66% and the load drop is correspondingly 65%. Note that the measurement of the actual drop in load from the load record, that is, the precise location of points a and b in Figure 8, takes into account the resonance in the system that occurs immediately after the spall for a brief period.

In summary we note the following similarities between previous tests and the present ones. 1. Regions of intact ice exist where the pressure is high at the ice/platen interface. 2. Melting, and flow of the melt in a thin layer at the high-pressure contact interface occurs. 3. Rapid relative displacement of the platen/ice occurs during load drops. This is caused by spalling at the intact ice/platen interface. Consequently much higher rates of melting and liquid flow occur at the load drops than at other times during the crushing tests.

The primary difference observed between previous experiments and the present test results was that the sawtooth load pattern, due to cyclic spall events, was not evident in these tests, although spalls did occur from time to time. This is likely the result of the confinement differences. Since spalling was not prevalent in the present tests the penetration was continuous for the most part, i.e. at the nominal rate of platen penetration, whereas when cyclic spalling occurs, as in previous tests, the actual penetration rate on the ascending portions of the sawtooth load is lower than the nominal rate, or negligible, due to compliance of the ice/indentor system.

The mechanism responsible for the majority of the energy dissipation, however, is the same in the present and previous studies, namely melting and viscous flow of melt (Gagnon, 1999).

CONCLUSIONS

A new type of ice crushing experiment has been conducted that enables a unique side-viewing perspective of the ice behavior.

The important phenomena of melting, due to viscous flow of a thin layer of high-pressure liquid at the ice/structure interface, and spalling at the ice contact zone have been observed in unprecedented detail. The frequency of spall events in the present tests is much less than is normally observed in ice crushing, probably due to the very different confinement aspects of the test setup.

As in previous crushing experiments, high-speed video has proven to be a very useful data acquisition system and an invaluable tool for interpretation of the results.

It would be very instructive to conduct similar tests at larger scales.

ACKNOWLEDGEMENTS

The author would like to thank the Program of Energy Research and Development (PERD) for their financial support of this research.

REFERENCES

Evans, A.G., Palmer, A.C., Goodman, D.J., Ashby, M.F., Hutchison, J.W., Ponter, A.R.S. and Williams, G.J. 1984. Indentation spalling of edge-loaded ice sheets. *IAHR Ice Symposium*, Hamburg, 113-121.

Faraday, M. 1859. On regelation, and on the conservation of force. *Phil. Mag*. 17, 162-169.

Fransson, L., Olofsson, T. and Sandkvist, J. 1991. Observations of the Failure Process in Ice Blocks Crushed by a Flat Indentor. *Proceedings of the 11th International Conference on Port and Ocean Engineering Under Arctic Conditions*, St. John's, Canada, Vol. 1, 501-514.

Frederking, R., Jordaan, I.J. and McCallum, J.S. 1990. Field Tests of Ice Indentation at Medium Scale, Hobson's Choice Ice Island, 1989. *Proceedings of the 10th International Symposium on Ice (IAHR 90)*, Espoo, Finland, Vol. 2, 931-944.

Gagnon, R.E. 1994a. Generation of Melt During Crushing Experiments on Freshwater Ice. *Cold Regions Science and Technology*, Vol. 22, No. 4, 385-398.

Gagnon, R.E. 1994b. Melt Layer Thickness Measurements During Crushing Experiments on Freshwater Ice. *Journal of Glaciology*, 1994, Vol. 40, No. 134, 119-124.

Gagnon, R.E. 1998. Analysis of Visual Data from Medium Scale Indentation Experiments at Hobson's Choice Ice Island. *Cold Regions Science and Technology*, Vol. 28, 45-58.

Gagnon, R.E. 1999. Consistent Observations of Ice Crushing in Laboratory Tests and Field Experiments Covering Three Orders of Magnitude in Scale. *Proceedings of the 15th International Conference on Port and Ocean Engineering under Arctic Conditions*, POAC-99, Helsinki, Finland, Vol. 2, 858-869.

Gagnon, R.E. and Mølgaard, J. 1991. Evidence for pressure melting and heat generation by viscous flow of liquid in indentation and impact experiments on ice. *Proceedings of the IGS Symposium on Ice-Ocean Dynamics and Mechanics*, 1990, New Hampshire, Ann. of Glaciol., 15: 254-260.

Gagnon, R.E. and Sinha, N.K. 1991. Energy Dissipation Through Melting in Large Scale Indentation Experiments on Multi-Year Sea Ice. *Proc. of the 10th International Conference on Offshore Mechanics and Arctic Engineering*, Stavanger, Vol. IV, Arctic/Polar Technology, 157-161.

Määttänen, M. 1983. Dynamic ice-structure interaction during continuous crushing. *CRREL Rep*. 83-85.

Masterson, D.M., Frederking, R.M.W., Jordaan, I.J. and Spencer, P.A. 1993. Description of multi-year ice indentation tests at Hobson's Choice Ice Island - 1990. *Proceedings of the 12th International Conference on Offshore Mechanics and Arctic Engineering*, Vol. 4, 145-155.

Michel, B. and Blanchet, D. 1983. Indentation of an S2 floating ice sheet in the brittle range. *Ann. Glaciol.*, 4: 180-187.

Riska, K., Rantala, H. and Joensuu, A. 1990. Full scale observations of ship-ice contact. Laboratory of Naval Architecture and Marine Engineering, *Helsinki University of Technology*, Report M-97.

Sodhi, D.S. and Morris, C.E. 1984. Ice forces on rigid, vertical, cylindrical structures. *CRREL Rep.* 84-33.

Timco, G.W. and Jordaan, I.J. 1988. Time series variations in ice crushing. *Proceedings of the 9th International Conference on Port and Ocean Engineering Under Arctic Conditions*, Fairbanks, Alaska, 13-20.

Wilson, C.J. 1999. Downloadable movie from the website of the School of Earth Sciences - The University of Melbourne - Australia. Copyright Notice - The University of Melbourne, 1994 - (2000). http://web.earthsci.unimelb.edu.au/wilson/ice1/index.html

17th International Symposium on Ice
Saint Petersburg, Russia, 21-25 June 2004
International Association of Hydraulic Engineering and Research

IN-SITU FRACTURE OF FIRST-YEAR SEA ICE IN McMURDO SOUND

John P. Dempsey[1], Zonglei Mu[1] and David M. Cole[2]

ABSTRACT

The breakup of sea ice in McMurdo Sound has been studied during two field trips in the fall of 2000 and 2001 via in-situ cyclic loading and fracture experiments. In Cole et al. (2002), the motivation, test site, experimental setup, cyclic response and associated acoustic emission for the 5 ×5 m^2 test specimen A2-SP2 were presented. In Dempsey et al. (2003), the fictitious crack model, which makes uses of the stress-separation curve, was used to incorporate a process zone into the fracture analysis. The cracking behavior observed and measured on A2-SP2, during both the cyclic loading and the displacement controlled ramp to tensile fracture was examined. Preliminary estimates of the fracture energy were provided. In this paper, stress-separation curves for the A2-SP2 experiment are constructed such that the response computed using the fictitious crack model matches the experimental results. A bilinear stress-separation curve is back-calculated for first-year Antarctic sea ice. The changing shape of the stress separation curve during crack growth is studied. It is hypothesized that this change is reflective of a multiple crack path competitive process.

ACRONYMS

CMOD	crack-mouth-opening-displacement
COD	intermediate-crack-opening-displacement
CTOD	crack-tip-opening-displacement
FCM	fictitious crack model
FPZ	fracture process zone
NCTOD	near-crack-tip-opening-displacement

INTRODUCTION

The breakup of floating first-year Antarctic sea ice is investigated in this paper, with the goal of developing improved, physically based models of this important process. Two field trips have been conducted in McMurdo Sound, Antarctica in support of this objective.

[1] Clarkson University, Potsdam, New York, USA
[2] US Army ERDC-CRREL, Hanover, New Hampshire, USA

The in-situ experiments conducted during the October-November 2001 field trip were located at S 77° 35.033′ E 166° 06.005′, approximately 3 km offshore from Cape Barne on Ross Island. Cole et al. (2002) described the test site, experiment setup and methods used in the in-situ experiments on the through-thickness specimen A2-SP2 of first-year sea ice measuring 5×5 m^2, and presented results for the cyclic loading response, acoustic emission activity and physical properties. Once the constitutive testing was completed, the specimen was loaded to failure in either load or displacement control to obtain its fracture behavior. Dempsey et al. (2003) then concentrated on the fracture behavior measured and observed in the same specimen A2-SP2. Several separate tests of A2-SP2 were examined and a preliminary estimate of the critical crack-tip-opening-displacement was found. In order to meaningfully interpret the fracture results, the fictitious crack model (FCM) was adopted to describe the fracture of A2-SP2. Hillerborg et al. (1976) first proposed this cohesive zone model for the fracture of concrete. It is a nonlinear cohesive zone model that includes the tension softening process zone through a fictitious crack (without complete separation of the crack faces) ahead of the traction-free crack. In the fictitious crack it is possible to distinguish two zones: a real crack where there are no tractions, and a damaged zone, denoted as the fracture process zone (FPZ), in which stresses are still transferred. The response of material points lying in the fracture process zone is governed by the stress-separation curve, which relates the opening of the crack faces w to the cohesive stress σ_{fpz}. As such, the stress-separation curve $\sigma_{fpz}(w)$ and the area under this curve G_c are the fundamental properties defining the fracture. In the present paper, an effort is made to deduce the stress-separation curve by matching the response of the fractured specimen with that from the fictitious crack model such that the distribution of cohesive stress within the process zone for any geometry and crack size is known.

THE FRACTURE OF A2-SP2

The in-situ fracture test discussed in this paper is the 5 m square plate of sea ice labeled A2-SP2 (Figure 1). The test configuration is shown in Figure 1a. All dimensions are in cm. The LVDT ranges (± ranges) are in microns. Both a ‘coarse range’ ($_c$) and a ‘fine range’ ($_f$) gage were used to record the crack-mouth-opening-displacement (CMOD), intermediate-crack-opening-displacement (COD), and near-crack-tip-opening-displacement (NCTOD). The notation NCTOD$^{\pm}$ indicates that the LVDT concerned was placed 10 cm ahead of ($^+$) or before ($^-$) the crack tip. So-called ‘fictitious’ gages (F1, F2 and F3) were also placed ahead of the crack tip to identify the crack-opening-displacement when the crack advanced.

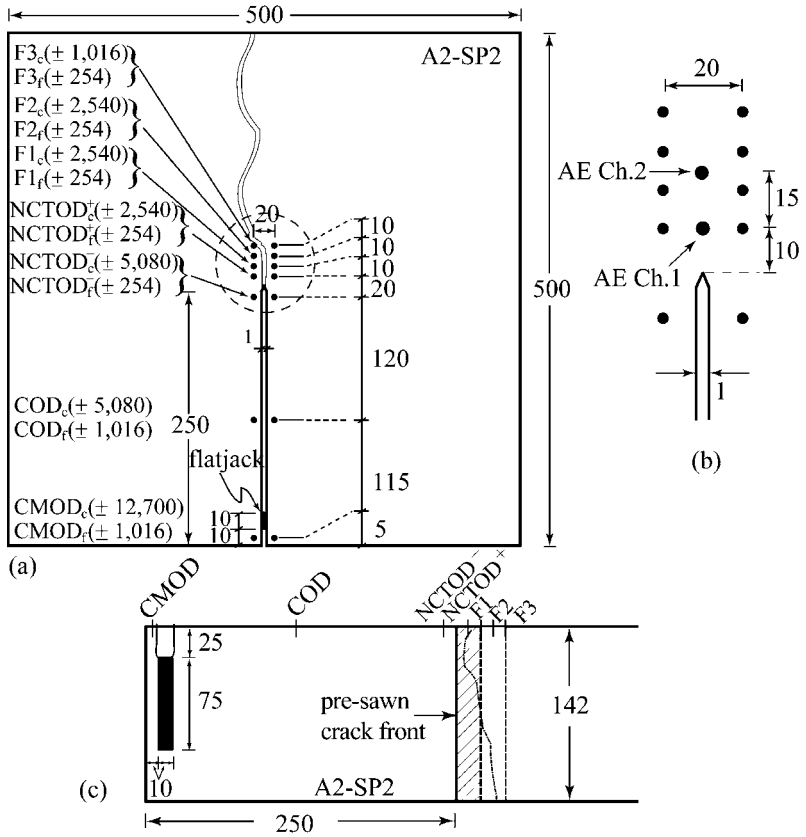

Fig. 1. a) The test configuration for A2-SP2; b) closer look at LVDT and AE sensor locations ahead of the crack tip; c) Side view of the pre-sawn crack, flatjack placement, and schematic of the crack front

Experimental results and discussion

As described in Dempsey et al. (2003), even though many of tests of A2-SP2 were targeting the cyclic behavior of the first-year sea ice, the cyclic loading also induced cracking in the vicinity of the traction-free crack tip. As A2-SP2 was subjected to more and more cycles, it was possible to follow the growth of the FPZ. The fracture behavior of Tests #4, #6 and #7 were thoroughly examined by Dempsey et al. (2003).

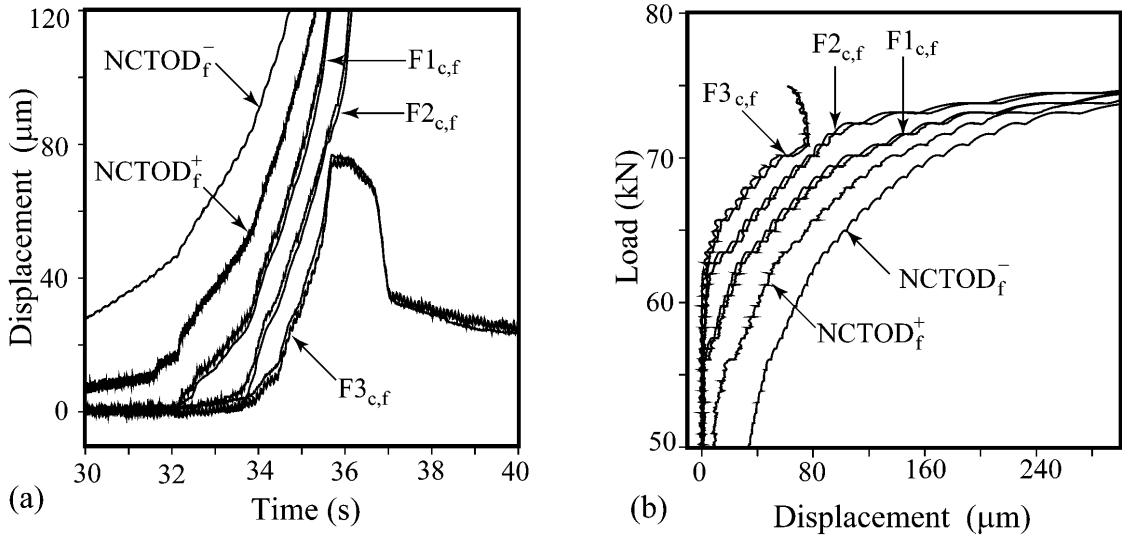

Fig. 2. Test #15: a) NCTOD$^{\pm}$, F1, F2 and F3 vs time; b) Load vs NCTOD$^{\pm}$, F1, F2 and F3

In Test #15, the objective was to stably fracture the 5m square test piece. Therefore, in displacement control, the CMOD was subjected to a sine-curve-shaped ramp versus time such that tensile failure would occur in less than 50 s (the peak load of 76.2 kN occurred at 36.8 s). The load and crack-opening-displacement behavior at some of the gages are portrayed in Figure 2. Note that the fracture behavior of this first-year sea ice in McMurdo Sound was studied by measuring the crack-opening-displacements at the surface only. It is an especially difficult matter to determine what the critical separation (w_c) for this ice is. In other words, what is the critical CTOD for growth of the traction-free crack to initiate? When the crack did propagate, it veered to the left slightly, just passing to the left of the F3 gage (see the crack path in Figure 3). In Figure 2a, note that the F3 versus time plot shows a sudden relaxation; this occurs at t= 35.7 s, at an opening load of 72 kN, and at a gage separation of 77 μm. The interpretation is that a FPZ had been getting established straight ahead of the traction-free crack path, in addition to a FPZ on the final crack path, until suddenly crack growth along the final path was found to be easier (no doubt due to a mild alignment of the ice fabric at the test site). For this reason, one can hypothesize that $w_c > 77$ μm. Until one sees crack-opening-displacements of this magnitude in the FPZ, growth of the traction-free crack is not likely.

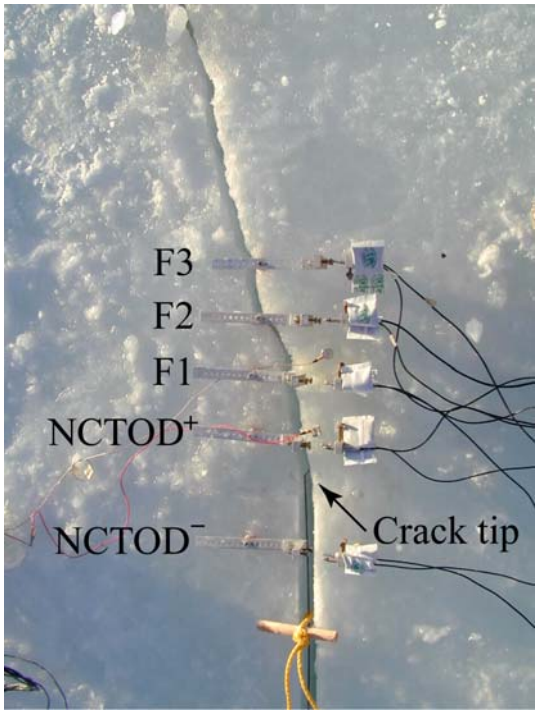

Fig. 3. Crack path of A2-SP2 after test

Modeling the experimental response

In the fictitious crack model, the stress separation and specimen material behavior can be modeled as viscoelastic. For the present set of experiments, the stress-separation curve as well as the viscoelastic characterization of the sea ice is not known. Moreover, it does not seem possible to conduct direct tension in-situ experiments in the field to experimentally obtain these material parameters. However, this information can be back-calculated such that predicted results match the experimental results. Dempsey and Mulmule (1998) developed a viscoelastic fictitious crack model for the fracture of sea

ice. The same procedure is used here to carry out the match between the model and experiment. Figure 4 shows a representative set of results for A2-SP2. To ensure the accuracy of the iteration procedure, the loading must be applied at the same rate as during the experiment. Figure 4a shows the experimentally applied load and the load applied to the model. Due to unexpected indentation of the flatjack, the initial loading actually began around 20kN. Figure 4b shows experimental crack opening displacements compared to the matched response of the model: at about 36s, the crack-tip-opening-displacement (CTOD) may reach the critical-crack-tip-opening-displacement before instability occurs because of stable crack growth.

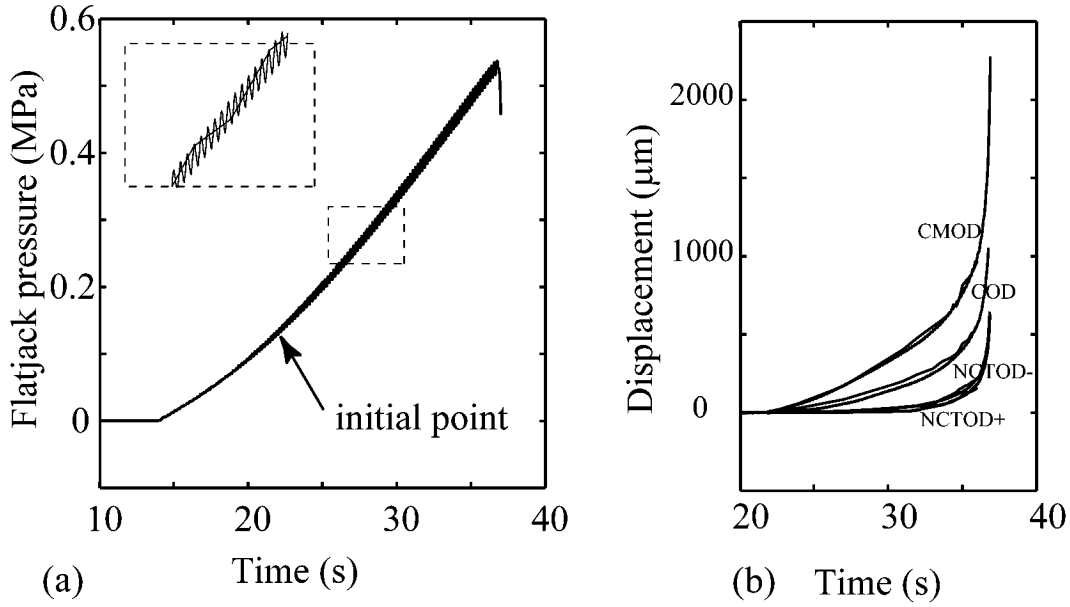

Fig. 4. Comparison of the experimental and matched (a) flatjack pressure vs time; (b) crack-opening-displacement vs time

Many different shapes of stress-separation curves have been used for different materials. Figure 5a shows various shapes of stress-separation curves that have been proposed. Shape ABC is the Dugdale distribution with a cutoff (see page 161 in Bažant and Planas, 1998). Shape AC is linear softening (a common approximation). Shape AEC is the concave bilinear shape that is found for concrete (Guinea et al. 1994). For the first-year sea ice discussed in this paper, Figure 5b shows the back-calculated stress-separation curve for A2-SP2 that is applicable prior to growth of the traction-free crack. Note that a convex bilinear shape is needed, as was also found by Mulmule and Dempsey (1999) for colder Arctic ice. The creep compliance expression used to match the experimental and model results for A2-SP2 is $J=1/E+Ct^{1/2}$, where E=3.1 GPa and $C=3.5\times10^{-11}$ $m^2/Ns^{1/2}$. The critical CTOD obtained from the stress-separation curve is 80 μm; this also matched the preliminary estimate discussed above. The critical CTOD for the Antarctic A2-SP2 test is larger than that of Arctic ice, while the tensile strength is smaller. These changes may well be caused by the warm weather under which the A2-SP2 specimen exhibited more ductile behavior. Under such circumstances, the effective length of the crack may increase. The fictitious crack model theory explains the larger critical CTOD. The critical fracture energy to initiate stable propagation of the traction-free crack (13 J/m^2) in A2-SP2 is slightly smaller than its colder Arctic counterpart (15 J/m^2). The fully-grown size of the process zone in A2-SP2 is about 190 mm.

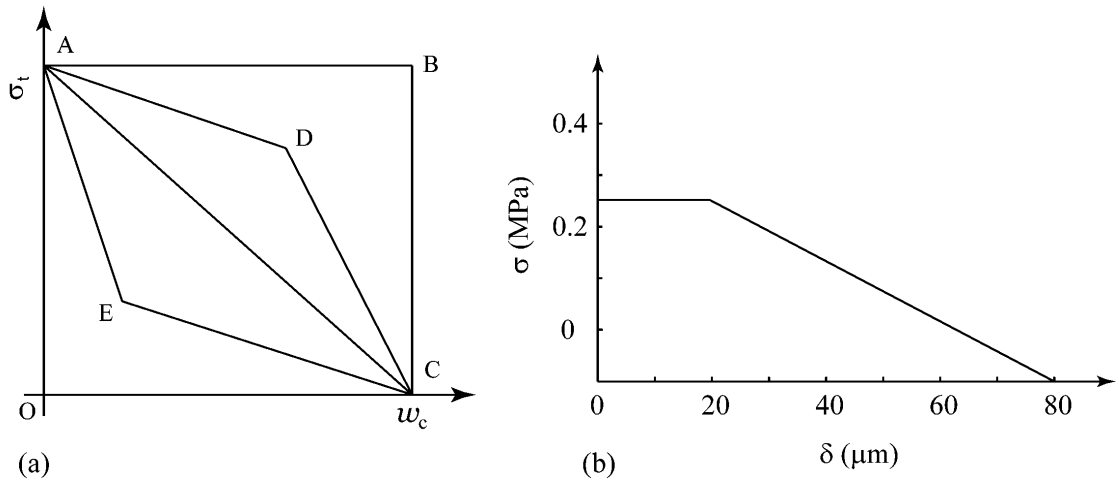

Fig. 5. (a) Various stress-separation curve shapes applicable for different materials;
(b) Back-calculated stress-separation curve for A2-SP2

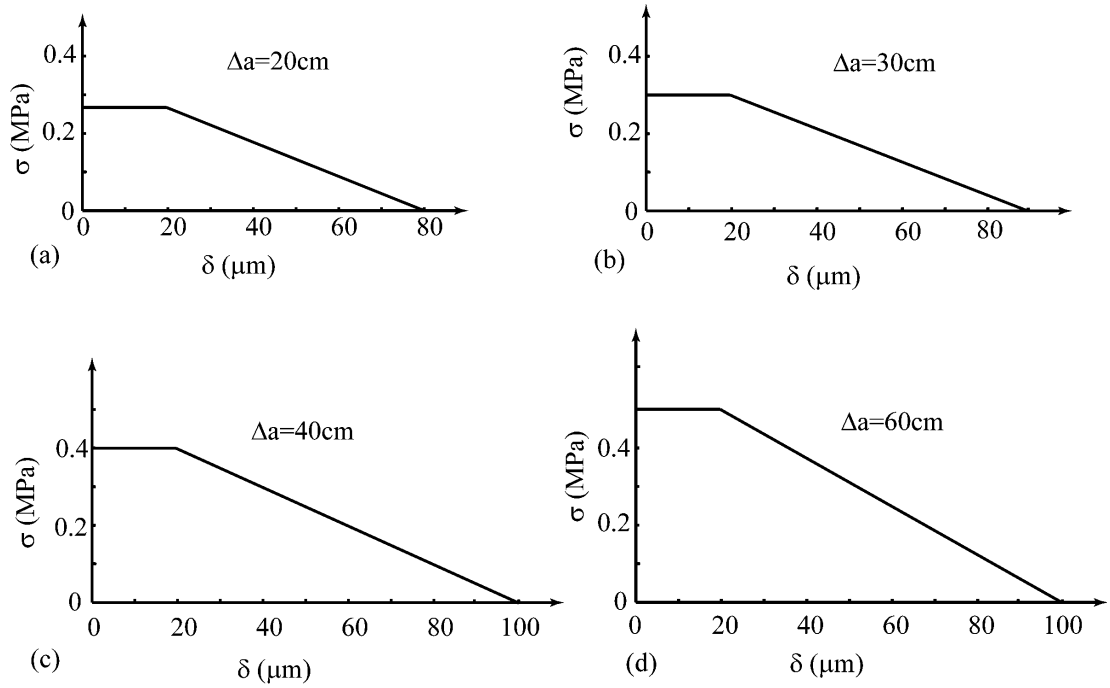

Fig. 6. Back-calculated stress-separation curves for A2-SP2 with growth of traction-free crack

In order to investigate how crack growth affects the fracture description, a number of stress curves were constructed, each associated with a specific amount of growth of the traction-free crack. These curves are shown in Figure 6. The behavior is indicative of an increase in fracture energy with crack propagation (Figure 7a). Post-test observations showed that the propagating crack seeks out planes of weakness within the microstructure, either following favorably oriented plate boundaries or larger-scaled brine drainage features. Branches were observed to run from the main crack and terminate at distances of approximately 0.1 m from the crack face. These branches were frequently associated with brine drainage features. Occasionally, a crack branch would rejoin the main crack and thereby break sections of material free of the crack face. These post-test observations indicated that observed changes in the stress-separation behavior with crack growth may be reflective of a multiple crack path competitive process. With increasing

crack growth, the tensile strength and critical CTOD is increasing. The fictitious crack model predicts a decreasing size of the process zone with crack growth (Figure 7b).

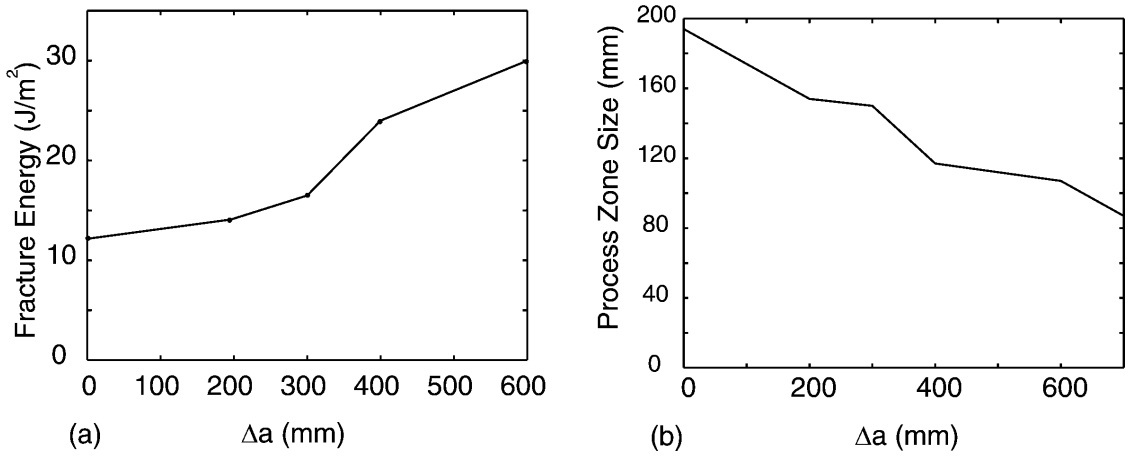

Fig. 7. (a) Fracture energy vs stable crack growth for A2-SP2;
(b) Decreasing fracture process zone length with crack growth

CONCLUSIONS

The experimental measurements and numerical calculations presented in the foregoing lead to the following observations:

1. Hillerborg's fictitious crack model can be applied to the fracture of floating first-year sea ice in Antarctica. The stress-separation curve for first-year Antarctic sea ice is convex and bilinear.

2. The length of the fracture process zone decreases with crack growth. A change in the stress-separation behavior with crack growth is reflective of a multiple crack path competitive process.

SIGNIFICANCE

The significance of the above findings rests with the resulting ability to predict the formation and behavior of a tensile crack in first-year sea ice. The fictitious crack model can describe the formation of a crack in an unnotched configuration, the growth of this crack to any extent, and the influence of specimen size as well as geometry. That is, with the stress-separation curve at hand, and given a chosen test geometry, the specimen size effects to be expected can be accurately predicted (Mulmule and Dempsey, 1999).

ACKNOWLEDGEMENTS

The support of NSF's Antarctic Sciences Ocean and Climate Program, grants OPP-9873629 and OPP-9909100, and Dr. Bernhard Lettau, the program manager, are gratefully acknowledged.

REFERENCES

Bažant, Z.P. and Planas, J. Fracture and Size Effect in Concrete and Other Quasibrittle Materials. *CRC Press* (1998).

Cole, D.M., Dempsey, J.P., Kjestveit, G., Shapiro, S., Shapiro, L.H. and Morley, G.M. The cyclic and fracture response of sea ice in McMurdo Sound: observations from in-situ experiments. Part I. In *16th IAHR International Symposium on Ice*, Vol. 1, University of Otago, Dunedin, New Zealand (2002) 474-481.

Dempsey, J.P., Cole, D.M., Shapiro, S., Kjestveit, G., Shapiro, L.H. and Morley, G.M. The cyclic and fracture response of sea ice in McMurdo Sound. Part II. In *Proceedings of the 17th International Conference on Port and Ocean Engineering under Arctic Conditions*, Vol. 1, Trondheim, Norway (2003) 51-60.

Guinea, G.V., Planas, J. and Elices, M. A general bilinear fit for the softening curve of concrete. *Materials and Structures 27*: 99-105 (1994).

Hillerborg, A., Modéer, M., and Petersson, P.E. Analysis of crack information and crack growth in concrete by means of fracture mechanics and finite elements. *Cement and Concrete Research 6*: 773-781 (1976).

Mulmule, S.V. and Dempsey, J.P. A viscoelastic fictitious crack model for the fracture of sea ice. *Mechanics of Time-Dependent Materials 1*: 331-356 (1998).

Mulmule, S.V. and Dempsey, J.P. Scale effects on sea ice fracture. *Mechanics of Cohesive-Frictional Materials 4*: 505-524 (1999).

17th International Symposium on Ice
Saint Petersburg, Russia, 21-25 June 2004
International Association of Hydraulic Engineering and Research

ICE PRESSURE VARIATIONS DURING INDENTATION

R. Frederking[1]

ABSTRACT

The Japan Ocean Industry Association made available to the IAHR Ice Crushing Working Group one data file from a field test conducted February 4, 1999. An indenter 1.5 m wide by 0.5 m high, penetrated a sea ice sheet 168 mm thick at a rate of 3 mm/s for a total penetration of 1000 mm. The entire indenter face was covered with "tactile" sensor elements, each nominally 10 mm by 10 mm. Spatial distributions of local pressure were recorded throughout the test as well as the total load measured with a load cell. Detailed analysis of the results showed that the load cell and tactile sensors gave comparable results. The tactile sensors showed a "line-like" load distribution with only about 10 % of the ice edge in load-bearing contact. "Hot-spots" of high local pressure persisted for surprisingly long periods, up to 10 s. Local pressure variations tended to be synchronous, that is largely increasing and decreasing with global load.

INTRODUCTION

The nature of local ice pressure distributions during indentation has been a subject of interest for some time in ice mechanics. It is an important factor in developing an understanding of the ice failure process since this understanding provide one of the means of scaling-up small-scale laboratory and field measurements to scales needed for design of offshore structures and ship hull structures. Obtaining good measurement data on pressure within the contact area was always a problem. If the sensor area was large, the pressure was averaged over too large an area; if the sensor area was small, there were usually insufficient sensors to determine the distribution of pressures. Load cells to measure average pressures over areas as small as 10 mm dia. were employed in laboratory and field measurements (Masterson et al, 1999, Sayed et al, 1992). Local pressures as high as 80 MPa were measured on a 10 mm diameter sensor in indentation of multi-year ice (Frederking et all, 1990). Early work in Finland (Joensuu, 1988) initiated the use of PVDF sensors to almost completely cover the measurement area. Later this type of instrumentation was deployed for field indentation teats on multi-year (Masterson et al 1993) and pressures as high as 50 MPa were measured.

More recently the Japan Ocean Industries Association (JOIA) sponsored a project on Medium Scale Field Indentation Tests (MSFIT) of ice sheets which ranged in thickness

[1] Canadian Hydraulics Centre, National Research Council Canada, Ottawa, Ont. K1A 0R6 Canada

from 120 mm to 270 mm. During the JOIA project detailed measurements of total load, loads on segments and local pressure distributions were made. The objective of the project was to obtain high quality data that could be used to improve the prediction of ice loads on structures. A general description of the test equipment and testing procedure can be found in Nakazawa et al (1999). To encourage broader understanding of the results, JOIA made available one data file to the IAHR Ice Crushing Working Group for analysis. These are the data examined in this paper. Spatial and temporal distributions of pressure will be examined, both on the basis of average distributions, shape of contours, simultaneity and variations during load cycles. Implications for describing ice crushing processes will be discussed.

DESCRIPTION OF TEST

The MSFIT program was conducted over 5 winters in the late 1990s at Notoro fishing harbour on the North coast of Hokkaido Island, Japan. The data file, from a test conducted February 4, 1999 was for the following conditions:

Indenter width = 1500 mm
Indenter height = 500 mm
Ice thickness = 168 mm
Indenter speed = 3 mm/s
Total stroke = 1000 mm
Ice strength = 2.46 MPa.

The total load exerted by the actuator was measured with a load cell and recorded at a rate of 50 readings a second. The entire indenter face was covered with “tactile” sensor elements, each nominally 10 mm by 10 mm, for a total of 6336 sensor elements (144 elements across and 44 elements vertically). The ice was not thick enough to ensure contact with all the sensor elements, but about 2500 elements contacted the ice edge. Data from the tactile film was recorded at a rate of one “frame” every 0.2667 s (3.7 Hz). A “frame” comprised a 144 by 44 matrix of “pressure” readings. Each element of the tactile film gave an integer reading between 0 and 255. The manufacturer of the film provided the following guide to convert output reading to pressure

reading	pressure (MPa)
0	0
55	0.68
255	6.86

with a linear relation. It was also stated that the error in any reading on the tactile film could be up to ± 10%, so it was recommended that pressure data be treated as relative.

The load record from the load cell is presented in Figure 1. It can be seen that there is rapid build-up of load to a high peak with the flat indenter making perfect contact with the flat sawed edge of the ice sheet. Using the indenter width of 1500 mm and the 168 mm ice thickness, the average pressure to initially fail the ice sheet was almost 3 MPa. Subsequently the average pressure was never greater than 0.5 MPa. The test was run at a constant actuator rate of 3 mm/s for 300 s (50 s is equivalent to 150 mm indentation). Immediately after the initial failure, fluctuations in the load were small. For the interval 40 to 70 seconds (Figure 2), the fluctuations were still small with a pattern of a general rise followed by a rapid drop off with an irregular period of 5 to 10 seconds. At around 80 seconds (Figure 3) the fluctuations settled into a more regular pattern with a frequency of about 1.2 Hz and the peak-to-trough ratio of the amplitude about 2. It can be

seen that the nature of the load fluctuations changes significantly between the two time intervals (Figures 2 and 3). The pattern demonstrated in Figure 3 tended to persist for the remainder of the test. Also shown in Figure 2 and 3 is a total load determined from the tactile film records. This will be discussed further.

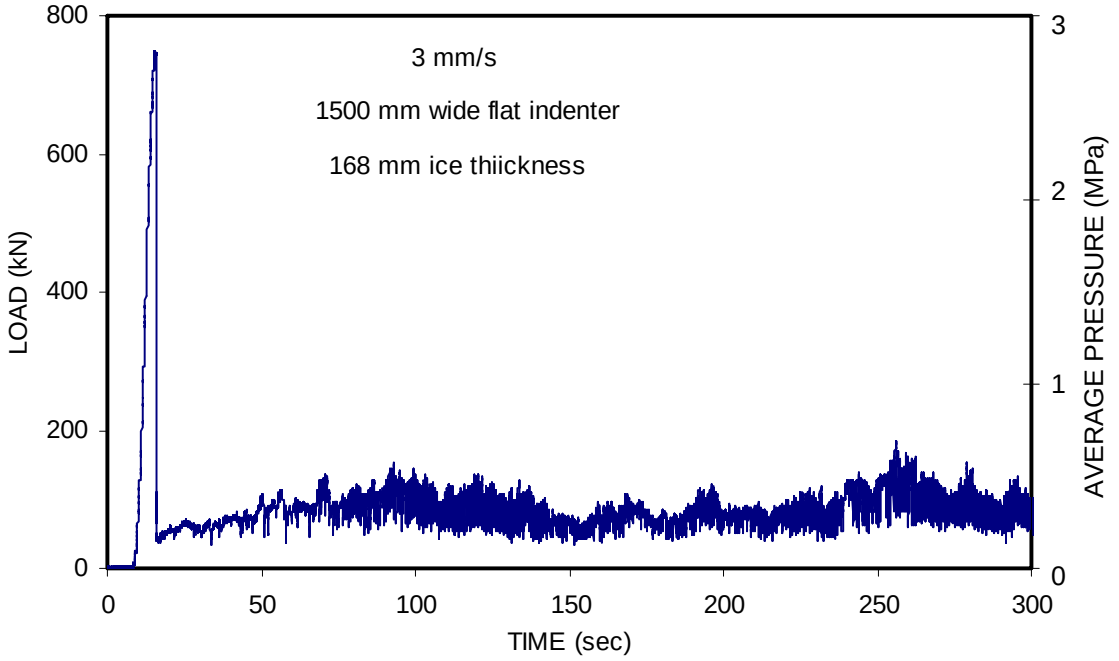

Fig. 1. Load – time record for test on February 2, 1999

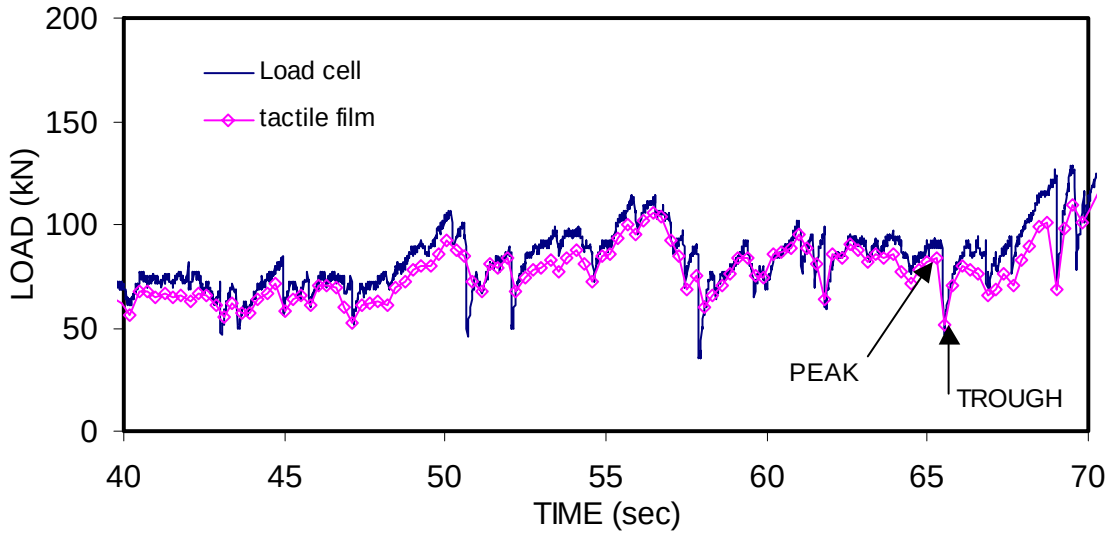

Fig. 2. Load – time record expanded for interval 40 to 70 seconds

The tactile film data were used to determine total load using a rather simple method of assigning a load of 1 N per reading unit; that is, a reading of 10 is equivalent to 10 N. Thus the total load in kN is just the sum of all tactile cell readings divided by 1000. This is the method used to obtain the tactile film loads presented in Figures 2 and 3. The recording frequency of the tactile film determined loads is much less than the load cell, approximately 4 Hz versus 50 Hz, but the tactile film traces follow the trend of the load

cell determined loads quite closely. Different recording systems were used so the load drop from the initial failure was used as an initial synchronizing point, but no further synchronization was used throughout. This basis to calculate total load implies a pressure of 2.55 MPa for a reading of 255, rather than the value of 6.8 MPa given by the manufacturer, and again emphasizes that pressures be treated a relative, not absolute.

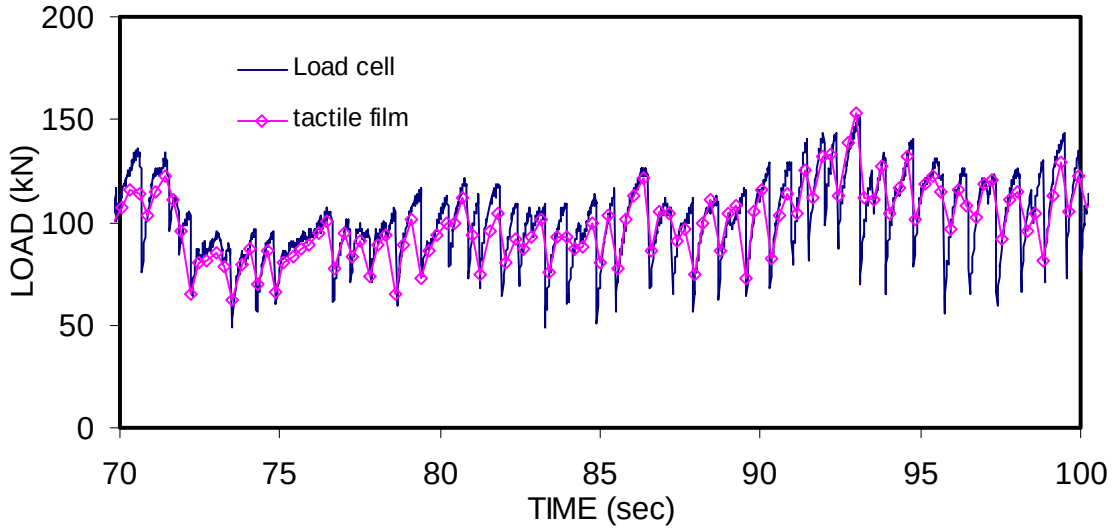

Fig. 3. Load – time record expanded for interval 70 to 100 seconds

DISTRIBUTIONS OF PRESSURE

The nature of ice pressure distributions at different points in the loading process will be examined next. At the 65 second mark (see Figure 2) two successive tactile film records were selected, one at 65.26 s just before failure, “peak”, followed by one at 65.53 s, just after failure, “trough”. The nature of, and change between the two will be discussed. The total loads at the two times, as estimated from the tactile film, are 85 kN and 53 kN, respectively, about a 40% decrease. Contour plots of the two times for the entire ice edge in contact with the indenter (168 mm by 1500 mm) are presented in Figure 4. The values plotted are the pressure numbers, within the range 0 to 255, from the tactile film record (note; all subsequent plots and discussion treat pressure as unitless). What can be seen firstly is that the area subjected to ice pressure is greater at the peak than the trough (290 elements at the peak and 255 at the trough), a 10% decrease so this alone does not account for the magnitude of the decrease. Note that the total possible number of cells in contact with the ice edge is 2448, so only about 10% are actually loaded. The number of cells subjected to ice pressures greater than 10, 25, 50 and 75 was determined and the greatest difference between the two cases was for pressures greater than 50 (see Table 1). At the peak there were 57 cells above that level, but only 15 at the trough. A number of vertical profiles of pressure were also examined, and they showed that generally the distribution was peakier at peak load than in the trough. Two immediately adjacent vertical pressure profiles at peak and trough are shown in Figure 5 to illustrate this point.

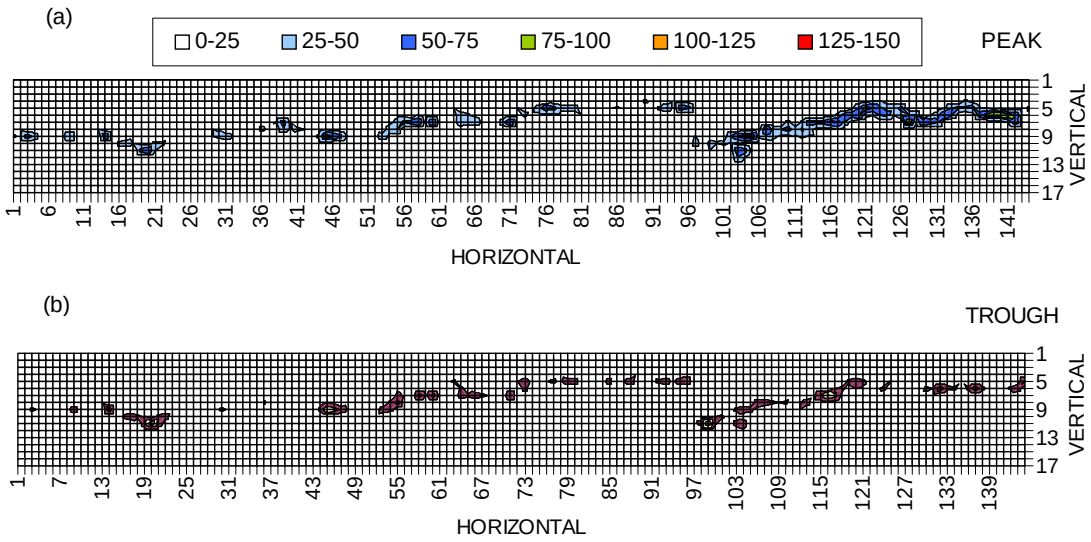

Fig. 4. Contour plots of pressure at 65 s; (a) peak, (b) trough

Table 1. Number of tactile elements loaded at 65 s

Pressure range	Peak	Trough
> 0	291	255
0 to 10	69	85
10 to 25	97	95
25 to 50	68	60
50 to 75	37	12
>75	20	3

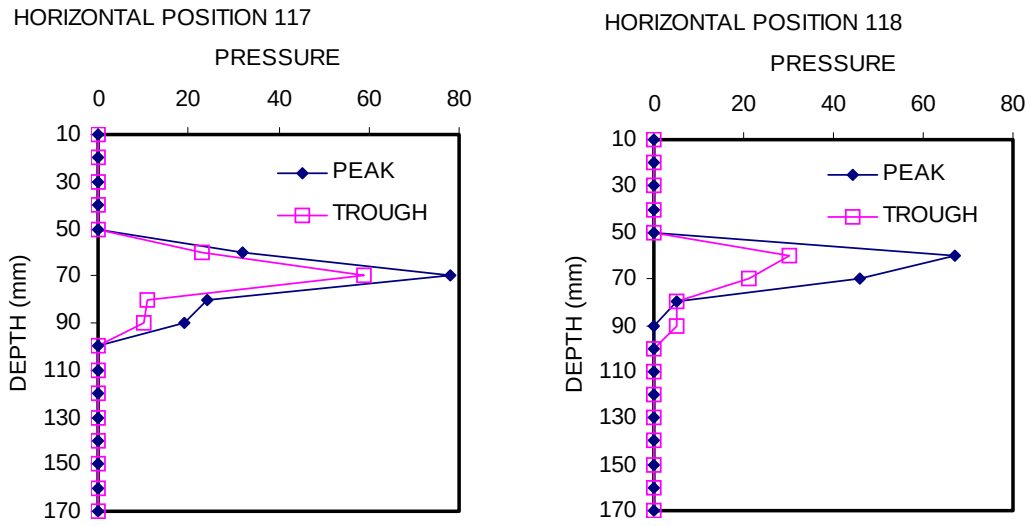

Fig. 5. Vertical pressure distributions at 65 s

Figure 6 presents the horizontal distribution of pressure summed on a vertical axis for the whole width of the indenter. It can be seen that for the most part the two pressure distributions are of similar magnitude for both the peak and trough. It is only for horizontal positions 100 to 140 that the total peak pressures are greater.

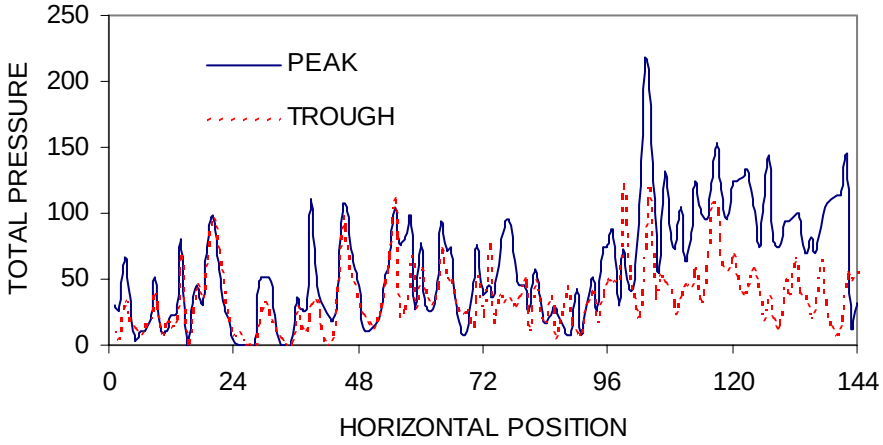

Fig. 6. Total pressure along a vertical line of elements at 65 s

As was shown in Figure 4, the line-like load distribution was generally not continuous across the entire width of the indenter, even at the time of peak load. What was also observed at some times was a double peak in the vertical distribution of pressure. Figure 7 plots six immediately adjacent vertical pressure profiles, covering a width of 60 mm, and all show similar double peaks. This double peak is likely a measurable representation of horizontal cleavage cracks that have been observed in indentation tests. A contour plot of the area from which the vertical profiles of Figure 7 were extracted (Figure 8) more clearly illustrates two line-like loaded areas. Figure 8 also illustrates that the high pressure between horizontal positions 100 and 120 has persisted for 5 seconds. In fact, this high pressure area or “hot spot” persists to a greater or lesser extent for the entire test run.

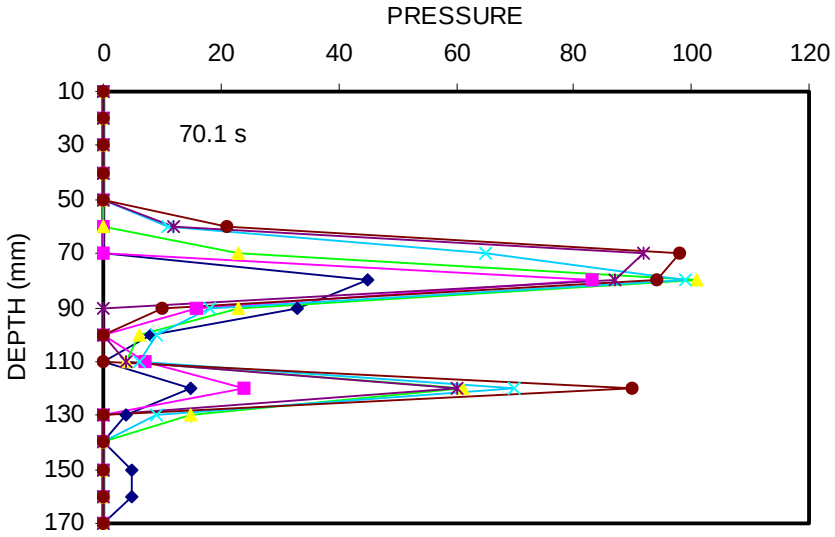

Fig. 7. Vertical pressure distributions at 70.1 s

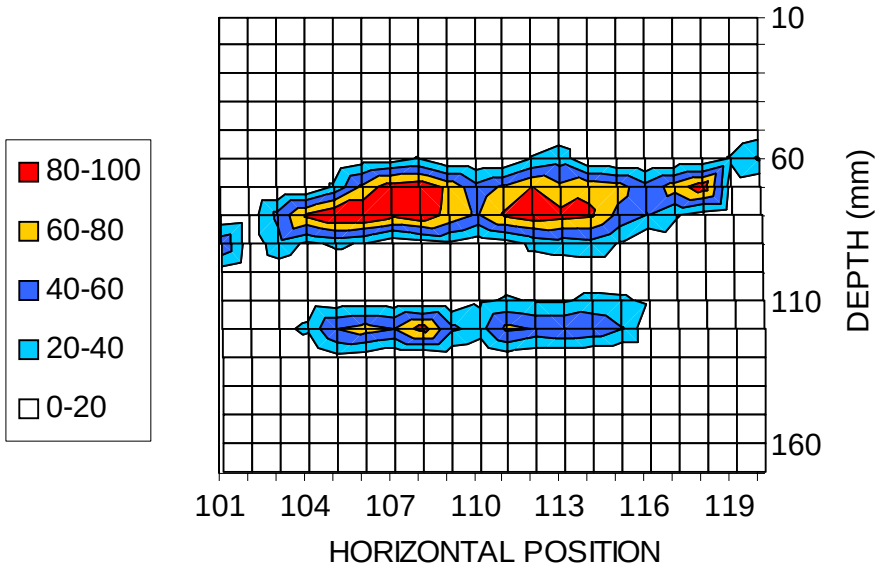

Fig. 8. Contour plot of pressure distribution at 70.1 s

To illustrate further pressure distributions and persistence of “hot spots” a contour plot at time 86.1 s is presented in Figure 9. Here there are three horizontal line-like loads and the high pressure areas are still evident in the horizontal position area 100 to 140.

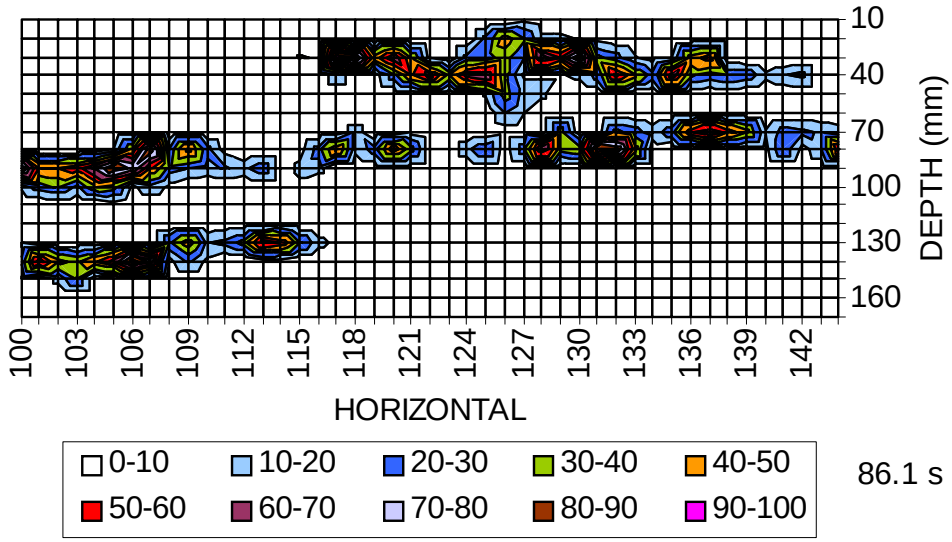

Fig. 9. Contour plot of pressure at time 86.1 s, a time of peak load

SUMMARY

An indentation test at 3 mm/s on 168 mm thick sea ice provided detailed information on pressure distributions through use of “tactile” file sensor elements covering the entire face of the 1500 mm wide indenter. Summing the tactile sensor data gave total loads similar to those from a load cell that measured total load. The tactile sensors showed a “line-like” load distribution with only about 10 % of the ice edge experiencing any local pressure at all. Local pressure distribution before and after failure indicated that the contact area was essentially the same in both cases, but that there was a larger area of high pressure just before failure. The line-like load distribution was observed to divide into

two or more horizontal parallel lines, suggesting cleave crack formation. “Hot-spots” of high local pressure persisted for surprisingly long periods, say up to 10 s, and tended to be in the middle portion of the ice edge.

ACKNOWELDGEMENTS

The author would like to acknowledge the financial support for this work from the Program of Energy Research and Development (PERD) through the ice-structure interaction activity, and the Japan Ocean Industry Association for making these data available.

REFERENCES

Frederking, R., Jordaan, I.J. and McCallum, J.S. 1990. Field Tests of Ice Indentation at Medium Scale, Hobson's Choice Ice Island, 1989. Proc. *IAHR 10th International Symposium on Ice*. August 20-23, 1990. Espoo, Finland, Vol. 2. pp. 931-944.

Joensuu, A. 1988. Ice Pressure Measurements using PCDF Film. *Proceedings 7th International Conference on Offshore Mechanics and Arctic Engineering (OMAE 1988)*, Houston, February 7-12, 1988, Vol. IV, p. 153-158.

Masterson, D.M., Spencer, P.A., Nevel, D.E. and Nordgren, R.P. 1999. Velocity Effects From Multi-Year Ice Tests. *18th International Conference on Offshore Mechanics and Arctic Engineering*, OMAE99, St. John's Newfoundland.

Masterson, D.M., Frederking, R.M.W., Jordaan, Ian J., and Spencer, Paul A. 1993. Description of Multi-Year Ice Indentation Tests at Hobson's Choice Ice Island - 1990. *Proceeding of the 12th International Conference on Offshore Mechanics and Arctic Engineering*, (OMAE 1993), June 20-24, 1993, Vol. IV, pp 145-155, Glasgow, Scotland.

Nakazawa, N., Akagawa, S., Kawamura, M., Sakai, M., Matsushita, H., Terashima, T., Takeuchi, T., Saeki, H. and Hirayama, H. 1999. Medium Scale Field Ice Indentation Test (MSFIT) – Results of 1998 Winter Tests. *Proceedings 9th (1999) International Offshore and Polar Engineering Conference*, May 30 – June 4, 1999, Vol. II, pp 498-504 Brest, France.

Sayed, M. and Frederking R. 1992. Two-dimensional Extrusion of crushed ice. Part 1: Experimental. Cold *Regions Science and Technology*, Vol. 21, pp 25-36.

17th International Symposium on Ice
Saint Petersburg, Russia, 21-25 June 2004
International Association of Hydraulic Engineering and Research

POST-TERMINAL COMPRESSIVE DEFORMATION OF ICE: FRICTION ALONG COULOMBIC SHEAR FAULTS

A.Fortt[1] and E.M. Schulson[1]

ABSTRACT

Coulombic shear faults characterize terminal failure when polycrystalline ice Ih is rapidly loaded under a moderate degree of confinement. Post-terminal deformation occurs through frictional sliding along the shear fault. To examine this latter stage of deformation, experiments were performed on freshwater S2 ice at -10^{o} C. The ice was proportionally loaded biaxially across the column-shaped grains along a variety of all-compressive loading paths at four sliding velocities (8×10^{-1}, 8×10^{-2}, 8×10^{-3} and 8×10^{-4} mm/s.). At each velocity Coulomb's law describes the relationship between the shear strength of the fault and the normal stress across it, both at the onset of sliding and once sliding has progressed a few millimeters. The friction coefficient decreases with increasing velocity in a manner similar to that seen by Kennedy et al. (2000) in ice-on-ice experiments, but is higher by about a factor of two to four, depending upon the sliding velocity. The difference is attributed to surface roughness.

INTRODUCTION

The compressive behavior of S2 ice has been extensively studied (for review, see Schulson, 2001) in response to the need to predict forces on engineered offshore structures from ice sheets pushing on them. Forces exerted by, and thus on the sheets, are dependent on environmental conditions, such as the wind/ocean currents. The rate at which these forces develop, in turn, dictates whether the ice deforms in either a brittle or a ductile manner. Coulombic shear faults denote brittle behavior, which occurs when the ice deforms at a rate greater than a critical value (Schulson, 2001) and results in fractured ice. Under compressive loading the fragments slide past one another against frictional resistance. Understanding that resistance is important to predicting the movement of these fragments. The purpose of this paper, therefore, is to describe the results of experiments aimed at evaluating the frictional resistance to sliding, following terminal failure via Coulombic faulting.

EXPERIMENTAL PROCEDURES

Experiments were performed on fresh-water S2 columnar ice, grown in the laboratory, using established procedures described by Smith and Schulson (1993). In S2 ice the caxes of the hexagonal unit cell are randomly oriented in a plane perpendicular to the

[1] Thayer School of Engineering, Dartmouth College, Hanover, NH

long axes of the columns (Michel, 1978). The microstructure of the ice is shown in Fig. 1, along with the reference co-ordinate system. Plate-shaped specimens were cut from a parent sheet into prisms with dimensions along X_1 and X_2 of 160 mm and of thickness through X_3 of 50 mm, with all surfaces parallel to a tolerance of ± 0.1 mm. All experiments were conducted inside a cold room at –10 ± 0.2°C using a multi-axial testing machine (MATS), in two stages. The first stage consisted of creating a shear fault within the specimen, Fig. 2a, 2b, and the second stage, of sliding along the fault, Fig 2c, 2d.

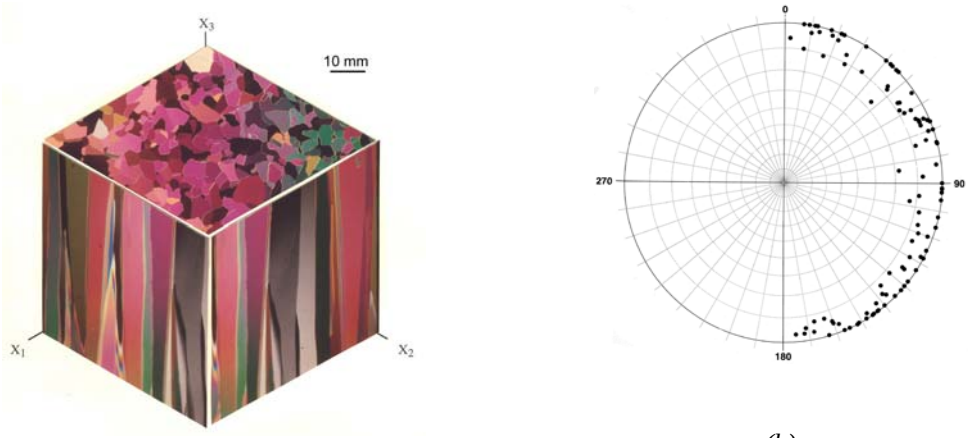

(a) *(b)*

Fig. 1. *(a)* S2 Ice. *(b)* The crystallographic orientation of C-axes with respect to the horizontal plane of the parent puck, plotted on a Wulff net

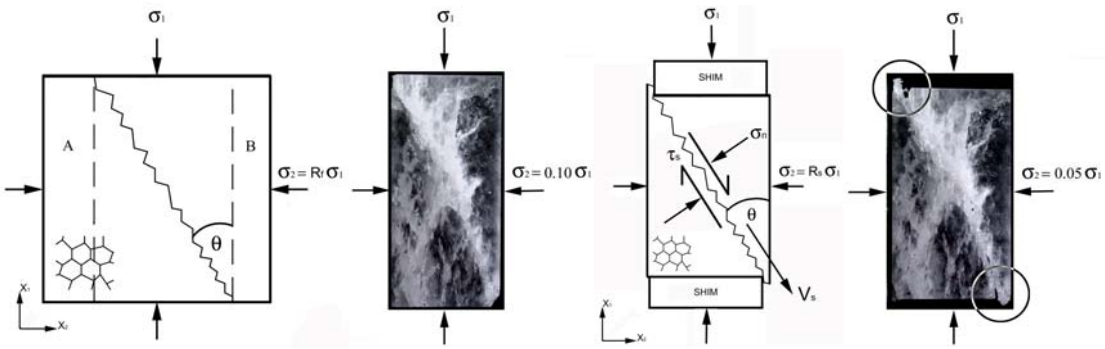

(a) *(b)* *(c)* *(d)*

Fig. 2**.** *(a)* Schematic representation of faulting stage. *(b)* Illustration showing faulted specimen after re-machining specimen end parts A & B (shown in *(a)*). *(c)* Schematic representation of moment-free sliding. *(d)* Illustration showing the same specimen after sliding 8 mm at a velocity of 8×10^{-2} mm/s. Note the displacement at the end of the fault (circled). Scale: height of specimen = 160 mm.

Faulting. The procedure for the faulting stage was the same as the one used by Iliescu (2000) and described by Fortt et al. (2002) (Fig. 2a, 2b). Biaxial compressive loads were applied proportionally across the columns along directions X_1 and X_2, via polished brass platens, at an applied strain rate, $\dot{\varepsilon}_1 = 4 \pm 1 \times 10^{-3}\ s^{-1}$. The minor horizontal load was slaved to the vertical major load. The ratio of the minor stress, σ_2, to the major stress,

σ_1, is termed the confinement ratio, $R_f = \sigma_2/\sigma_1$, and was held constant during each test. All faults were introduced at essentially the same confinement, $R_f = 0.09 \pm 0.03$.

Sliding. The procedure for the sliding stage is the same as described in Fortt et al. (2002) except for one major difference. In brief, the faulted specimen was removed carefully from the MATS to avoid de-cohesion. Shims, 20 mm thick of polished brass, were then placed on the vertical platens in the major compressive stress direction as shown in Fig. 2c to allow the specimen to slide along the fault without crushing. The difference is that in the preliminary experiments (Fortt et al. 2002), shims were aligned with the center of the fault zone. This loading situation induced a moment and it was discovered that this moment significantly affected the results. Through careful handling of the specimen it was possible to cut and re-mill the ice so that the shims aligned with the edges of the specimen, thus eliminating the moment, as shown in Fig. 2c & 2d. All results reported below were obtained with moment-free sliding.

The specimens were deformed by sliding along the faults at four different sliding velocities, 8×10^{-1} mm/s, 8×10^{-2} mm/s, 8×10^{-3} mm/s and 8×10^{-4} mm/s. The largest imposed displacement was, $\delta \approx 8$ mm. The other variable was confinement, from $R_s = 0.05$ to 0.9, where the subscript denotes sliding.

The normal stress, $\sigma_{n,}$ and the shear stress, τ, on the sliding fault were calculated from the relationships:

$$\sigma_n = \sigma_1 \sin^2\theta + \sigma_2 \cos^2\theta, \quad (1a)$$

$$\tau = (\sigma_1 - \sigma_2)\sin\theta\cos\theta, \quad (1b)$$

where θ is defined in Fig. 2.

RESULTS AND OBSERVATIONS

Fig. 3 shows typical stress vs. displacement curves collected for each velocity at the same confinement. Three kinds of behavior were observed, depending upon the sliding speed:

(i) 8×10^{-1} mm/s: At the highest displacement velocity and over the entire range of confinement the deformation was noisy (to the unaided ear). The applied stress increased, reached a maximum, and then dropped suddenly, followed by 'stick-slip' sliding (Fig. 3a). The magnitude of the 'stick-slip' peaks increased and the frequency decreased with increasing confinement.

(ii) 8×10^{-2} mm/s and 8×10^{-3} mm/s: At intermediate speeds the deformation was less noisy, but still audible. Stress vs. displacement curves (Fig.3b & 3c) were characterized by an initial rapid increase followed by a gradual rising to a rounded peak. There was no sudden-type failure as seen at the highest velocity; instead the stress gradually decreased.

(iv) 8×10^{-4} mm/s: At the lowest speed the deformation was quiet. Sliding was characterized by stress vs. displacement curves (Fig. 3d) without a 'peak-stress': the stress rose rapidly and then tended to level off. Deformed specimens showed evidence of fault healing: the faults possessed an opaque appearance after sliding compared to a highly cracked and fragmented appearance in the newly faulted specimen. Also after sliding the full 8 mm the specimens possessed greater integrity than specimens deformed at higher velocities. Evidence that the fault was still sliding could be seen in fracture features on opposite sides. By comparing photographs of the specimen before and after sliding, it could be seen that the two sides had moved relative to one another.

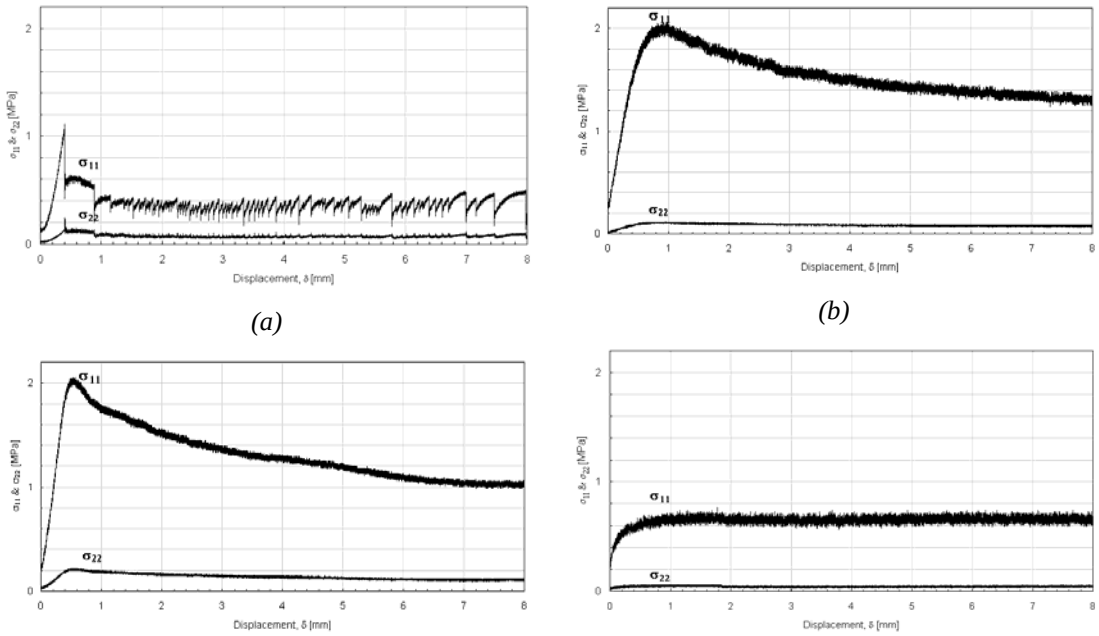

Fig.3. Stress versus displacement curves for specimens tested under a confinement ratio of $R_s \sim 0.09$ at *(a)* 8×10^{-1} mm/s *(b)* 8×10^{-2} mm/s *(c)* 8×10^{-3} mm/s *(d)* 8×10^{-4} mm/s sliding velocity

To obtain failure envelopes, four data points were taken from each stress-displacement plot, one at the onset of sliding and then at displacements of $\delta \approx 2.4$, 4.0 and 8.0 mm. Onset was taken to be the maximum stress from the displacement curves for the three highest velocities and from an extrapolation of the two near-linear regions for the lowest velocity (Fig. 3d). Figures 4 and 5 show the envelopes, for the onset of sliding and for the three post-onset displacements, respectively. Data are shown only for those confinements below a critical value, R_{crit}, listed for each velocity in Table 1. The critical loading path, R_{crit}, corresponds to the suppression of sliding in a direction along the fault, as discussed in Fortt et al. (2002).

Table 1. Parametric values for Equation 2. r^2 is the correlation coefficient. The units of τ_0 are MPa

		Onset of Sliding			**2.4 mm**			**4.0 mm**			**8.0 mm**		
Velocity (mm/s)	**R_{Crit}**	**τ_0**	**μ**	**r^2**	**τ_0**	**μ**	**r^2**	**τ_0**	**μ**	**r^2**	**τ_0**	**μ**	**r^2**
8×10^{-1}	0.19	0.06	**0.89**	*1.00*	0.00	**0.85**	*0.98*	0.02	**0.77**	*0.95*	0.01	**0.77**	*0.98*
8×10^{-2}	0.14	0.09	**1.06**	*0.99*	0.07	**1.04**	*1.00*	0.04	**1.07**	*1.00*	0.02	**1.07**	*0.99*
8×10^{-3}	0.09	0.02	**1.36**	*0.99*	0.02	**1.35**	*0.99*	0.02	**1.34**	*0.99*	0.02	**1.36**	*0.99*
8×10^{-4}	0.11	0.05	**1.17**	*0.97*	0.03	**1.26**	*0.96*	0.05	**1.15**	*0.98*	0.04	**1.20**	*0.98*

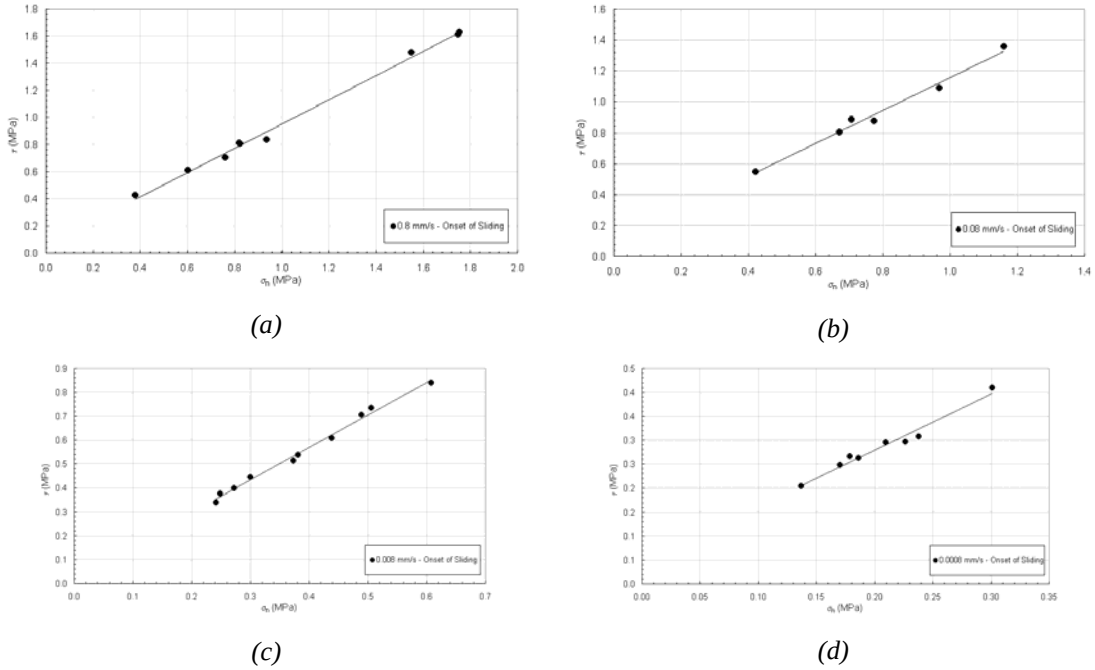

(a) *(b)*

(c) *(d)*

Fig. 4. Normal stress versus shear stress sliding failure envelopes at the onset of sliding for *(a)* 8×10^{-1} mm/s *(b)* 8×10^{-2} mm/s *(c)* 8×10^{-3} mm/s *(d)* 8×10^{-4} mm/s sliding velocity.
Note: Different scales on each graph

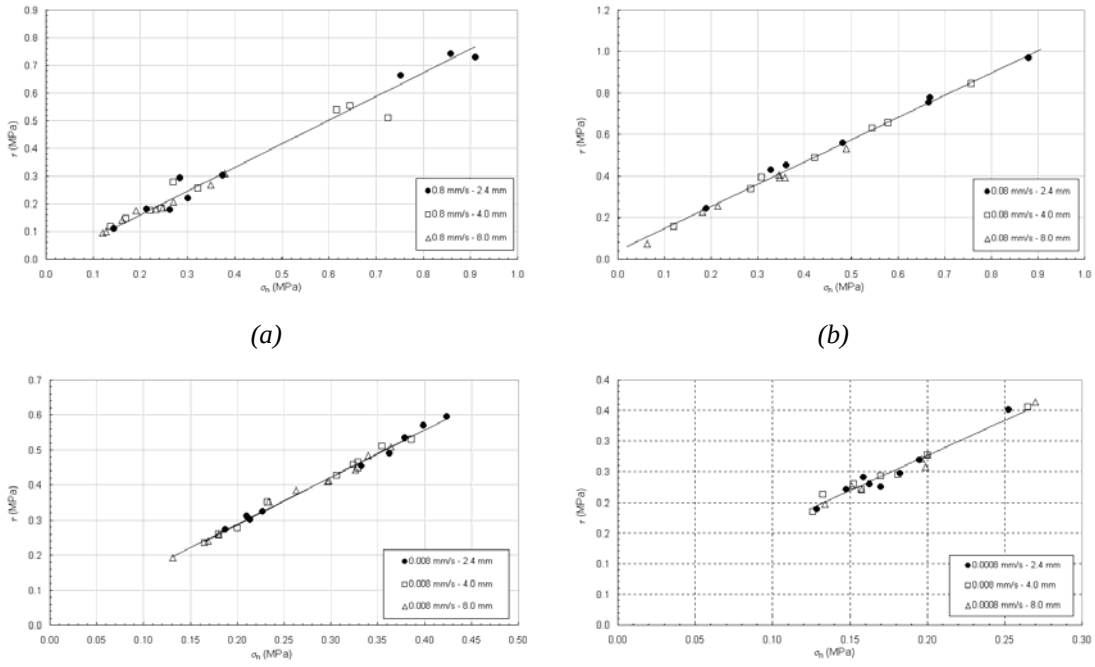

(a) *(b)*

(c) *(d)*

Fig. 5. Normal stress versus shear stress for sliding displacements of, $\delta \approx 2.4$, 4.0, 8.0 mm for *(a)* 8×10^{-1} mm/s *(b)* 8×10^{-2} mm/s *(c)* 8×10^{-3} mm/s *(d)* 8×10^{-4} mm/s sliding velocity.
Note: Different scales on each graph

The data show that the sliding resistance increases in a linear manner with increasing normal stress for both the onset of sliding and for its continuation. The relationship may be described by Coulomb's law:

$$\tau = \tau_0 + \mu\sigma_n, \tag{2}$$

where τ_0 is a measure of the cohesion of the fault and μ is the coefficient of friction. Table 1 lists the parametric values. All data appear to be well behaved and show a high correlation to Coulomb's law with $r^2 \geq 0.96$. Displacement appears to have little systematic effect on the friction coefficient, except perhaps at the highest velocity where the coefficient decreases slightly with displacement (Fig. 6). The friction coefficient decreases with increasing velocity in a manner similar to that seen by Kennedy et al. (2000) and Montagnat et al. (2004) in ice-on-ice experiments (Fig. 7). Our values of μ are higher by a factor of two to four, depending on the sliding velocity, than those reported for ice-on-ice experiments (Fig. 7).

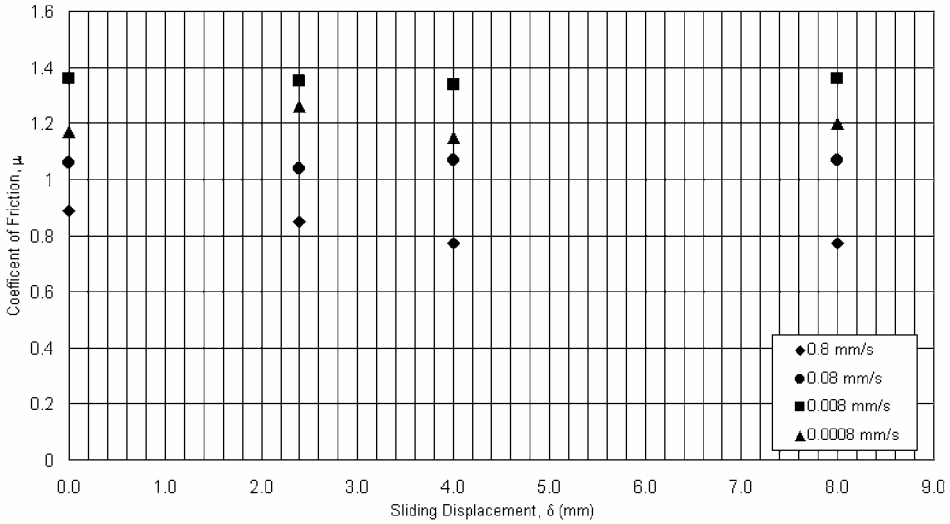

Fig. 6. Sliding displacement versus coefficient of friction

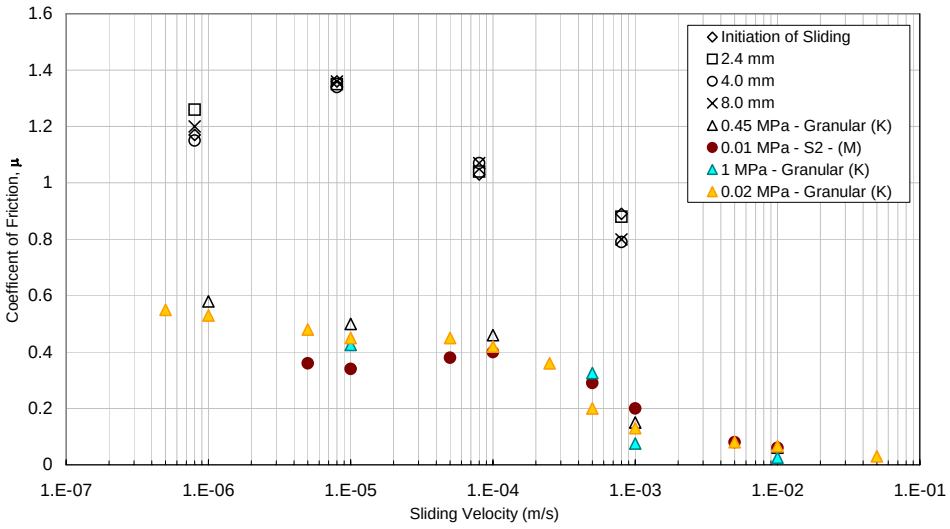

Fig. 7. Comparison between friction of Coulombic shear faults obtained here, with friction coefficients obtained from Kennedy et al. (2000) , denoted (K), and Montagnat et al. (2004), denoted (M)

DISCUSSION

It should be noted that "sliding" as used here is not taken to mean the kind of deformation that occurs when two bodies slide past each other across a clearly defined interface. Rather, it means deformation within a narrow band of damage (i.e., the fault). That kind of deformation probably consists of a complicated mixture of several processes, including interfacial sliding, fracture and melting and, at the lower speeds, creep and sintering. Regardless of the details, "sliding" may be viewed as localized, inelastic deformation under an applied shear strain rate $d\gamma/dt = V_s/ w$, where w is the thickness of the fault and V_s is the sliding velocity.

When viewed in the above light, some of the behavior revealed here can be understood within the broader context of the inelastic behavior of ice under compression. In the present experiments, the fault thickness was about two to three times the grain size, d, as evident in Figs. 2b and 2d, typical of Coulombic faults in fresh-water S2 ice (Illiescu, 2000). This means that the average strain rate (for a grainsize of 6 ± 3 mm) varied from $\sim 5 \times 10^{-5}$ s^{-1} at the lowest velocity to $\sim 5 \times 10^{-2}$ s^{-1} at the highest velocity. When intact ice is compressed at –10 ^{o}C at applied strain rates greater than $\sim 10^{-3}$ s^{-1}, it exhibits macroscopically brittle behavior, which is characterized by sudden load drops and by moderate strain-rate softening. When strained more slowly, it exhibits ductile behavior, which is characterized by strain-rate hardening. Thus, the change in the character of sliding seen appears to be the manifestation of a brittle-to-ductile transition.

The root of the high friction coefficients from Equation 2 in relation to prepared ice on ice (Fig. 7) likely lies in the interactions of asperities. Byerlee (1967) found that in rock friction increased from $\mu \sim 0.15$ for mirror-smooth surface, to $\mu \sim 0.6$ as the roughness increased, owing, he proposed to the increasing interlocking of asperities. A similar process may operate in ice.

CONCLUSIONS

From sliding experiments on naturally-formed Coulombic shear faults within fresh-water S2 ice loaded biaxially at –10°C, it is concluded that: (i) sliding exhibits brittle-like behavior at higher speeds (i.e., $> 8 \times 10^{-2}$ mm/s), whilst at lower speeds (e.g., 8×10^{-4} mm/s) it exhibits ductile-like behavior; and (ii) the shear resistance obeys Coulomb's law with μ increasing as velocity decreases within the 'brittle' regime.

ACKNOWLEDGEMENTS

The authors would like to acknowledge Dr. Daniel Iliescu for his help with the experiments. The work was supported by National Oceanographic and Atmospheric Administration, grant no. NA17RP1400, and the National Science Foundation, grant no. OPP-032 8605

REFERENCES

Byerlee, J.D., Theory of Friction based on Brittle Fracture, *J. Appl. Phys*, 38 (7), 2928, (1967).

Fortt, A, Schulson, E.M. and Russel, E, Sliding along Coulombic shear faults in ice, *Can. J. Phys*, 81, 519-527, (2003).

Illiescu, D. Contributions to Brittle Compressive Failure of Ice, *Ph. D Thesis*, Dartmouth College, Hanover, NH, (2000).

Kennedy, F.E, Schulson, E.M and Jones, D.E., The friction of ice on ice at low sliding velocities, *Philosophical Magazine A*, 80(5), 1093-1110, (2000).

Michel, B, Ice mechanics, *Laval University Press*, Quebec, Canada, p168, (1978).

Montagnat, M., and Schulson, E.M., On friction and surface cracking during sliding of ice on ice, *J. Glaciology*, 49(166), 391-396, (2003).

Schulson, E.M., Brittle failure of ice, *Eng. Fracture Mechanics*, 68(17-18), 1839-1887, (2001).

Smith, T.R. and Schulson, E.M., The brittle compressive failure of fresh-water columnar ice under biaxial loading, *Acta Metall. Mater.*, 41(1), 153-163, (1993).